Journal of Information Technology and Education Science

JITES

Published by:
University of Computer Studies (Taungoo)

December, 2020
Volume-02, Issue-01

JOURNAL OF INFORMATION TECHNOLOGY AND EDUCATION SCIENCE VOL. 02, ISSUE. 01, 2020

ISBN: 978-99971-0-928-6
Publisher: University of Computer Studies (Taungoo)

University of Computer Studies (Taungoo)
Yangon-Mandalay Road,
Taungoo Township,
Bago Region, Myanmar.

JOURNAL OF

INFORMATION TECHNOLOGY AND EDUCATION SCIENCE

JITES2020 VOL. 02, ISSUE. 01, 2020

UNIVERSITY OF COMPUTER STUDIES (TAUNGOO)

Journal of Information Technology and Education Science

Vol. 02, Issue. 01, 2020

Content

Information Technology

Education Science

Computational Mathematics

Natural Science

Language

Natural Science

Design and Construction of Android Phone Controlled Electrical Household Appliances

Thet Lwin Oo[1], Win San Win [2,] Hnin Ei Maung[3], Lwin Lwin Soe[4]
[1]Assistant Lecturer, U, Department of Physics, Mandalar University
[2]Assistant Professor, Dr, Department of Physics, Mandalar University
[3]Demonstrator, Dr, Department of Physics, Mandalar University
[4]Demonstrator, Daw, Department of Physics, Mandalar University
[1]thetlwinoo777@gmail.com, [2]winnsannwinn@gmail.com, [3]hnineimaung@gmail.com,
[4]lwinlwinsoe777@gmail.com

ABSTRACT: *Android phone controlled electrical household appliances is constructed to control electrical household appliances as android phone remote controller. The control section will be based on digital signal processing with arduino and android phone. The Bluetooth link section will also include in the android smart phone control feature. Android phone and controlled circuit can communicate with each other from short range via Bluetooth. The desired mobile application (apk) can be developed on the android studio 2.0 and interfaced with system from any compatible device. Commands to ON/OFF electrical device can be sent easily and quickly from the mobile device. And the information of the present working status can be displayed on the monitor of the android phone. Bluetooth module is used to receive the signal that transmits from android phone in the circuit. So the constructed system can safety control three output AC load lines with the six input user interfaces under the Bluetooth wireless personal area.*

Keywords: Arduino Uno; Bluetooth Module; Developing android application on Android Studio 2.0; Optocoupler-relay driver circuit1

1. INTRODUCTION

The android application (apk) which can be controlled electrical household appliances is developed on the android studio 2.0. This controlled circuit is constructed with four main sections. They are Android phone application, Bluetooth module, Arduino Uno, and electrical household appliances.

The controlled circuit is constructed with Arduino Uno and other electronic components. Arduino Uno is a microcontroller board based on the ATmega 328. Microcontrollers are intelligent electronic devices used to control and monitor devices in the real world. Microcontrollers are programmed devices. C programming language is used to program Arduino Uno (microcontroller). An android phone is an electronic wireless portable scientific device. It is used not only a controller unit but also receive and send voice and messages from other compatible devices. Android phones are programmed devices. The user interface and java programme is developed on the android studio for installing the application firmware in the android phone. Bluetooth is a networking technology aimed at low-powered, short range applications. Bluetooth module is used to receive the signal and data that transmits from android phone in the circuit. Electrical household appliances are controlled wirelessly with android phone under the Bluetooth wireless personal area.

2. GENERAL DESCRIPTIONS OF THE SOFTWARE AND CIRCUIT COMPONENTS

2.1. Main Feature of the Constructed System

The system consists of five main sections. They are android phone, Bluetooth section, supply section, main control section and relay section. The block diagram of the whole system is described in Figure.1.

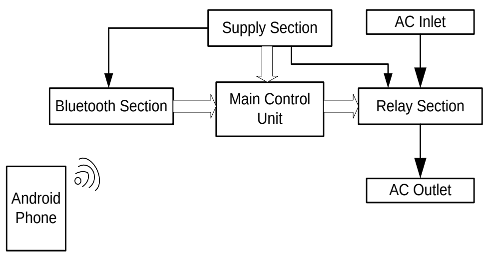

Figure 1. The block diagram of the whole system

The user control interfacing of android phone will be by means of virtual buttons of android phone for digital data signal processing. The Bluetooth section will communicate between android phone and arduino uno via Bluetooth link. The supply section will performs to generate the constant $+5V_{DC}$.The main control unit is responsible for accepting the Bluetooth interface data communication, supply section and for producing a suitable data signal to relay module section. The relay module section will use as switch for controlling AC load output. And the conditions of the latest AC load output will also display on the monitor of android phone.

2.2. Android Studio 2.0

Android Studio 2.0 is the fastest way to build high quality, performant apps for the Android platform, including phones and tablets, Android Auto, Android Wear, and Android TV. As the official IDE from Google, Android studio includes everything you need to build an app, including a code editor, code analysis tools, emulators and more. This new and stable version of Android Studio has fast build speeds and a fast emulator with support for the latest Android version and Google Play Services. Android Studio is built in coordination with the Android platform and supports all of the latest and greater APIs. It is available today as an easy download or update on the stable release channel. The logo of ANDROID STUDIO 2.0 software is shown in Figure.2.

Figure 2. The logo of ANDROID STUDIO 2.0 software

2.3. Arduino UNO

The 8-bit ATmega 328P microcontroller based Arduino UNO is used in the project to control different components like Bluetooth module and relay network, Android is an open-source operating system which means that any manufacture can use it in their phones free of charge; The board features 14 digital pins and 6 analog pins. It is programmable with the Arduino IDE via a type B USB cable. It can be powered by a USB cable or by an external 9 volt battery, though it accepts voltages between 7 and 20 volts. The hardware reference design is distributed under a Creative_Commons Attribution Share-Alike 2.5 license and is available on the Arduino website. Layout and production files for some versions of the hardware are also available. “UNO” means one in Italian and was chosen to mark the release of Arduino Software (IDE) were the reference versions of Arduino, now evolved to newer releases. The UNO board is the first in a series of USB Arduino boards and the reference model for the Arduino platform. The ATmega 328 on the Arduino Uno comes preprogrammed with a bootloader that allows to upload new code to it without the use of an external hardware programmer. It communicates using the original STK500 protocol. The UNO also differs from all preceding boards in that it does not use the FTDI USB to serial driver chip. Instead, it features the Atmega16U2 programmed as a USB to serial converter. The Arduino/Genuino board has a number of facilities for communicating with a computer, another Arduino/Genuino board or other microcontroller. The ATmega328 provides UART TTL (5V) serial communication, which is available on digital pins 0 (RX) and 1 (TX). An ATmega16U2 on the board channels this serial communication over USB and appear as a virtual com port to software on the computer. The 16U2 firmware uses the standard USB COM drivers, and no external driver is needed. However, on Windows, a .inf file is required. The Arduino Software (IDE) includes a serial monitor which allows simple textual data to be sent to and from the board. The RX and TX LEDs on the board will flash when data is being transmitted via the USB to serial chip and USB connection to the computer. A Software Serial library allows serial communications on any of the Uno’s digital pins. The photograph of ARDUINO UNO board is shown in Figure.3.

Figure 3. The photograph of the arduino UNO board

2.4. HC 05 Bluetooth Module

The HC 05 Bluetooth module is the most popular module in modern life and this module is mostly used in the embedded projects. The HC 05 Bluetooth modules are easy to use and simple, its price is low and these types of modules are interfaced with the arduino, Raspberry Pi, and Microcontroller through the serial UART interface. These modules are designed for the transparent wireless connection setup and it is very easy to use in the Bluetooth serial port protocol. The serial port, Bluetooth module is highly qualified Bluetooth with the version of the V2.0+Enhanced Data Rate of 3Mbps. The modulation has completely 2.4GHz radio transceiver and baseband. The pin diagram of HC 05 module is described in Figure.4.

Figure 4. The pin diagram of HC05 Bluetooth module

The HC 05 module is a MASTER/SLAVE module. By default the factory setting is SLAVE. The role of the module (MASTER or SLAVE) can be configured only by AT Commands. The SLAVE modules cannot initialize a connection to another Bluetooth device, but can accept connection. Master module can initialize a connection to another device. Some features of HC 05 Bluetooth module are as follows.

1. Slave default Baud rate: 9600, Data bits: 8, Stop bits: 1, Parity: No parity.
2. Auto-connect to the latest device on power as default.
3. Permit pairing device to connect as default.
4. Auto-pairing PINCODE “1234” as default.

2.5 Optocoupler-Relay Driver Circuit

The optocoupler-relay driver circuits is used to control various appliances and equipments with large current. It is equipped with high-current relays that work under AC250V 10A or DC30V 10A. It has a standard interfaced that can be controlled directly by Arduino Uno, Microcontroller, etc. The photograph of optocoupler-relay driver circuit is described in Figure.5.

Figure 5. The photograph of optocoupler- relay driver circuit

In this driver circuit, the relay is powered with separate circuit, this is one of a great task of optocoupler in electronic circuits. These circuit can be replaced by the LEDs placed in electronic circuits. It is very simple and using very few components which are optocoupler, transistor, relay and resistors. The optocoupler is a device which contains an LED and a phototransistor in a small package. They are manufactured in many different packages. The simple one contains one LED and one phototransistor which we have used in the circuit, other types contains many LEDs and phototransistors. When the power is applied to the LED in the photocoupler, the phototransistor receives the LED light and become switch ON. But the output of that transistor will not directly drive the relay. And then npn transistor will conduct and the relay coil will be electrified.

3. General Descriptions Of Android Section And The Constructed System

3.1. Android Section

The user interface or human-machine interface is the part of the machine that handles the human-machine interaction. The user interface can be accomplished by means of switches, variable resistors, capacitive touch pad and etc. Nowadays, the advanced way to control a machine is the applying an android phone. For our proposed system, the user interface feature will be included android phone control function using Bluetooth link. The program code for android is written with Java programming language.

Java is a general-purpose computer programming language designed to produce programs that will run on any computer system and android phone. The project title of this test work is taken as “ceremony application” and the software will generate the application firmware with this title. Since application programming interface level (API) in target android devices platform is setting API_21, these application firmware will run on approximately 85.0% of android phone that are active on Google Play Store. The function of our application firmware is to control the electrical household appliances. In this work, the program code is developed in steps for setting the size, design and position of the six virtual buttons, the currently working status on the android phone and for communicating with HC-05 module in Master-Slave mode configuration.

Before establishing communication between two Bluetooth devices, HC-05 module is needed to pair the android for communication. So the password for HC-05 module must be searched from Bluetooth of our android phone. If the Bluetooth device with “HC-05” name is found, it is needed to click on connect/pair device option and open our application firmware under the control of default baud rate (9600 bps). The six virtual buttons are defined to control the electrical household appliances. The virtual buttons (LD_1ON), (LD_2ON) and (LD_3) are used to switch ON the load respectively. Otherwise, the other three virtual buttons (LD_1OFF), (LD_2OFF) and (LD_3OFF) are also used to switch OFF the load respectively. The source code (.jav) file is converted to machine code (.apk) file using Android Studio software of version 2.0. The flow chart of the control program for data communication on android studio 2.0 is shown in Figure.6. The screenshot of “ceremony application” on android phone is described in Figure.7.

3.2. Regulated Power Supply Section

In the regulated power supply section, step-down transformer is used to obtain 12 V_{AC}. Full wave rectification is done using two 1N4007 diodes.A 1000 µF electrolytic capacitor is installed to perform as the main filter for eliminating the AC components. In order to get constant, +5 V_{DC} the voltage regulator chips 7805 is used electrolytic capacitors (100 µF) are installed at the regulated DC line. The circuit diagram of regulated power supply section is shown in Figure.8.

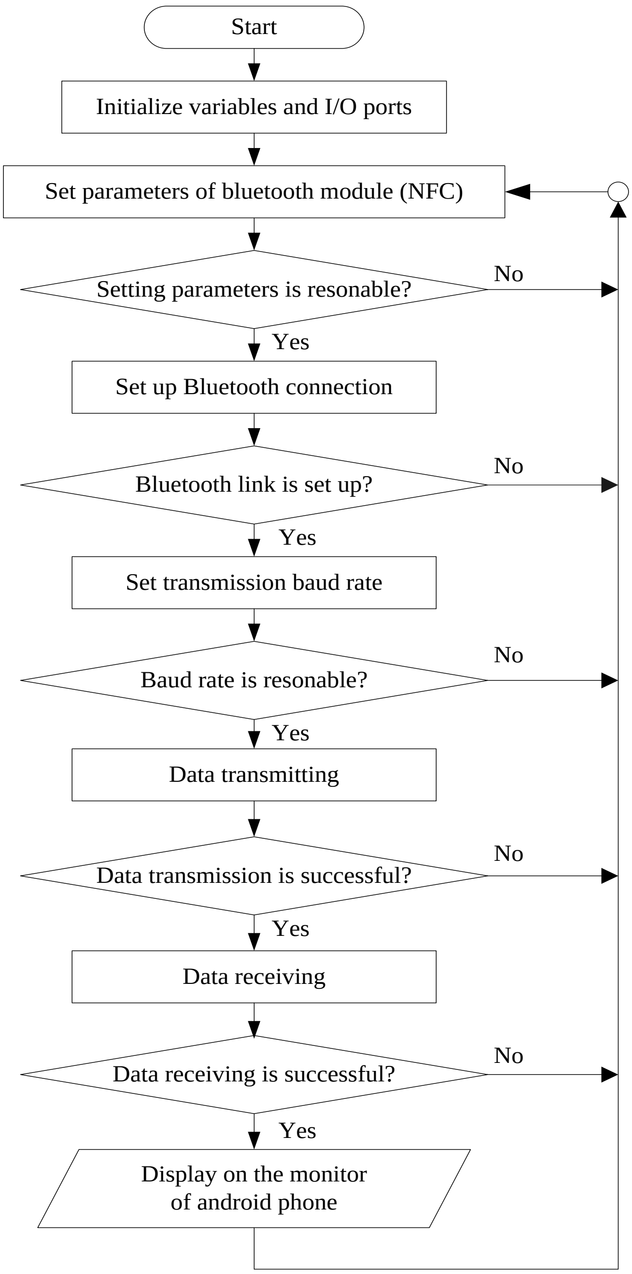

Figure 6. The flow chart of the control program for data communication

Figure 7. The screenshot of "ceremony application" on android phone

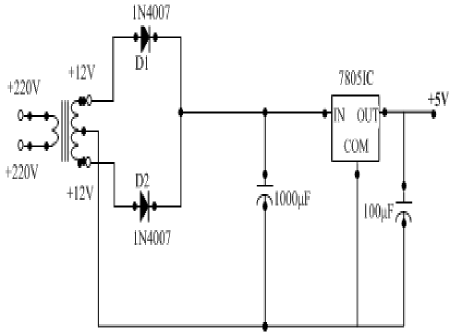

Figure 8. The circuit diagram of regulated power supply section

3.3 Control Section

The Android Phone Controlled Electrical Household Appliances is constructed by using Android phone, Bluetooth module, Arduino uno, transistor, optocoupler, relay, AC electric device, capacitors and resistors.Power (Barrel Jack) is connected to the regulated power supply using USB cable to power Arduino board. RX pin and TX pin of arduino UNO are connected to the TX pin and RX pin of Bluetooth module respectively. The TX pin of arduino board is used for sending the serial data into Android Phone and RX pin is also used to receive serial data from Android phone.The pin 13 of arduino board is connected to the pin1 of optocoupler. The pin 2 of optocoupler is connected to ground and pin 4 is connected to +5V power supply. The pin 3 of optocoupler is connected to the base of NPN transistor for biasing it. The collector of transistor is connected to the relay. The relay is connected to the load applied by AC 220V. The flowchart of the main control program of the system is described in Figure.9.

3.3.1. Operation of the System

When the application firmware (LED Controller) on the android phone is pressed, the bluetooth of android phone will open and search the other Bluetooth device under the range of Bluetooth automatically. If it searches the other Bluetooth device, the ON/OFF virtual buttons will appear on the screen of android phone. After searching the other Bluetooth device, TX led flashing of arduino board will stop and RX led flashing will run automatically. If the LD_1ON virtual buttons is pressed, the relay _1 is electrically closed. So load_1 reaches switching ON state. Instead of pressing ON virtual button, if LD_1OFF virtual button is pressed, the relay _1 is electrically opened, and the electric bulb reaches switching OFF state. And if LD_2ON virtual button and LD_3ON virtual button are pressed, the relay_2 and the relay_3 are electrically opened respectively. Otherwise, if LD_2OFF virtual button and LD_3OFF virtual button are pressed, the relay_2 and the relay_3 are also electrically opened respectively. The circuit of controlling the electrical household appliances by using Android Phone is shown in Figure.10. The internal circuit of the whole system is also shown in Figure.11.

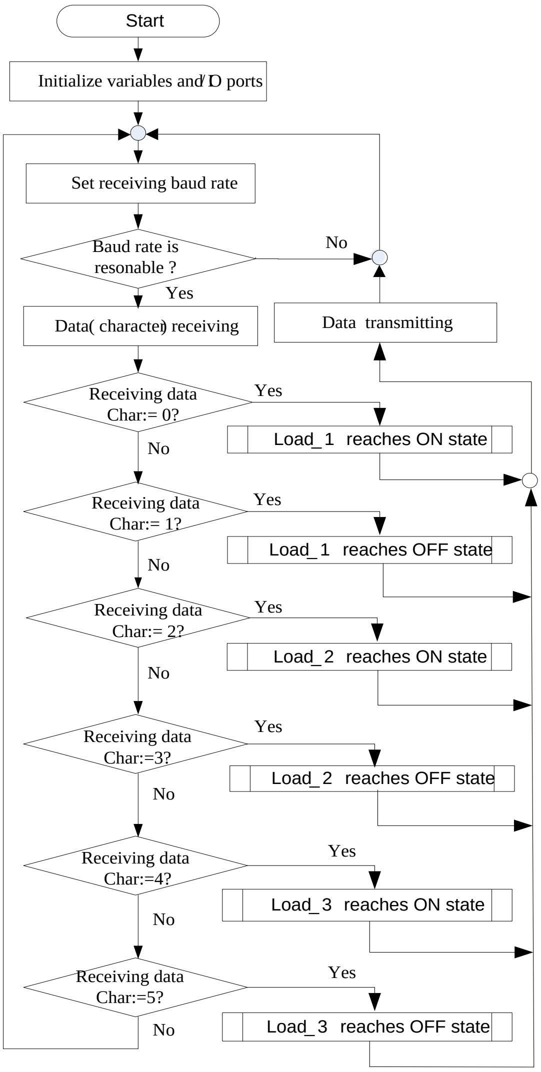

Figure 9. The flowchart of the main control program of the system

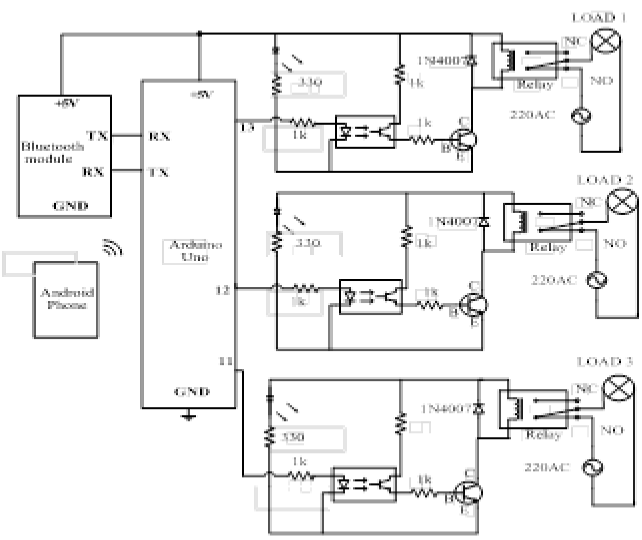

Figure 10. The circuit of controlling the electrical household appliances by using Android Phone

Figure 11. The internal circuit of the whole system

4. Abbrevations And Acronyms

apk: android application
IDE: Integrated Development Environment
UART: Universal Asynchronous Receiver-Transmitter
FTDI: Future Technology Device Interglobal
API: Application Programming Interface
TTL: Transistor-Transistor Logic

5. Result

Android phone controlled electrical household appliances has been constructed by using android phone, Bluetooth module and arduino board. The user interface and application firmware have been developed on the android studio 2.0 for setting the virtual button as described in Figure.12. The photograph of the experimental set up coupling with android phone is described in Figure.13. If LD_1ON virtual button, LD_ 2ON virtual button and LD_3ON virtual button are pressed, the load_1, load_2 and load 3 reach "ON" state respectively as shown in Figure.14.Otherwise, If LD_1OFF virtual button ,LD_2OFF virtual button and LD_3OFF virtual button are pressed, the load_1, load_2 and load 3 reach "OFF" state respectively as shown in Figure.15.

Figure 12. The photograph of the experimental set up coupling with android phone

Figure 13. The photograph of setting the virtual button on the android studio 2.0

Figure 14. The condition of the load_1, load_2 and load 3 reach "ON" state

Figure 15. The condition of the load_1, load_2 and load 3 reach "OFF" state

6. DISCUSSION

The constructed circuit is the circuit that controls AC equipments such as electric bulbs, fans etc with android phone. Since Bluetooth is a networking technology aimed at low-powered, short range application, and second classification of HC 05module so that we can control the home electrical appliances from a central location within maximum distance eleven metre wirelessly. But if the first classification of Bluetooth module, Wi-Fi module and GSM modem are used for controlling the home electrical appliances, we can completely control them away from the other places wirelessly. The system will be enhanced to control the speed of the fan or volume of the buzzer, android frequency counter etc for interfacing with sensors in future.

ACKNOWLEDGEMENT

I would like to express my gratitude to Dr Myin Zu Minn, Principal, Mandalar University, for her interest and encouragement on this research work. I particularly want to thank Dr San San Kyi, Professor and Head, Department of Physics, Mandalar University, for her advice and suggestions in this research work.

REFERENCES

[1] Andrew Hoog, "Android Forensics", Elsevier, United States of America (2011).

[2] Jessica Thorns, " Android UI Design, Production reference: 1180516" Birmingham B32PB, United Kingdom (2016).

[3] Macro Schwartz and Stefan Buttigieg, "Arduino Android Blueprints" Birmingham B32PB, United Kingdom (2014).

[4] Albert Rusell Van Cortlandt Warrington, "Protective Relays: Their Theory and Practice, Volume 2", London (1962).

[5] J.Ilett, "How to Use Intelligent LCDs", Everyday Practical Electronics Magazine, Camborne Publishing Ltd., United Kingdom (1997).

Construction of Motor Control System Using Fingerprint Sensor

Hla Thein Maung[1], Aung San Min[2], Aye Aye Khine[3]
[1]*Department of Physics, Shwebo University, Myanmar*
[2]*Department of Physics, Mandalay University of Distance Education, Myanmar*
[3]*Department of Physics, University of Myitkyina, Myanmar*
[1]*uhlatheinmaung465@gmail.com*, [2]*aungsanmin.phys.mdy@gmail.com*, [3]*draakmkn77@gmail.com*

ABSTRACT: *In the recent year, most door opening systems are controlled by the use of keys, password and security cards. Nowadays new technologies are improved, and the combination of hardware and software development is used for various embedded systems. Therefore, a motor control system is designed and constructed using fingerprint sensor. In the developed system, ATMEGA328P microcontroller is used as the main control and processing device of the whole system. An AS608 fingerprint sensor module is used to sense the fingers of people. A 2-line 16-character liquid crystal display (LCD) is used to show the information of the fingerprint. A DC 5 V motor is used to demonstrate the rotation and it is controlled by two relays. In this research, the developed system is tested by demonstrating motor rotation as clockwise and anticlockwise directions. The control program for ATMEGA328P microcontroller is written with C programming language and compiled by Arduino 1.8.12 software. The developed system can be used as fingerprint based door opening system or fingerprint based gate security system by attaching the motor at the door. The motor turns in clockwise direction when the finger of authorized people is placed on the fingerprint sensor. After 10 seconds, the motor turns in anticlockwise direction. The clockwise direction of the motor performs to open the door, and the anticlockwise direction of the motor performs to close the door. The time duration of the motor rotation can be changed by the control program. The fingerprint sensor used in this research is capable of storing up to 128 individual fingerprints.*

Keywords: fingerprint sensor; motor rotation; ATMEGA328 microcontroller; LCD

1. Introduction

Nowadays, there are many types of door openers available and they are passive infrared based door opener, radio frequency identification based door opener, and digital lock door opener. Fingerprint recognition is one of the most secure systems because a fingerprint of one person never matches with the others. Therefore unauthorized access can be restricted by designing a lock that stores the fingerprints of one or more authorized users and unlock the system when a match is found. Humans have used fingerprints for personal identification for many centuries and the matching accuracy using fingerprints has been shown to be very high, as in [1]. In this work, a fingerprint sensor based motor control system is designed and developed. The system can be installed at door entry. The fingerprint sensor is used to sense and also to determine the finger of authorized people or unauthorized people.

2. Brief Description Of The System

The constructed fingerprint sensor based motor control system consists of six main units and they are fingerprint sensor, power supply, main control and processing unit, liquid crystal display (LCD), direct current (DC) motor driver unit, and motor.

The functions of fingerprint sensor are to capture fingerprint image, to convert it into the equivalent template and also to save them into its memory on selected identification (ID) location. The functions of power supply are to provide 3.3 V for fingerprint sensor and 5 V for remaining units. The functions of main control and processing unit are to interface with fingerprint sensor, to control LCD, and to send the activation signals for DC motor driver unit. The function of LCD is to display the information of fingerprint. The function of DC motor driver unit is to control motor for rotating in clockwise direction and anticlockwise direction. The function of DC motor is to demonstrate the rotation of clockwise direction and anticlockwise direction. The block diagram of the constructed motor control system is shown in Figure 1.

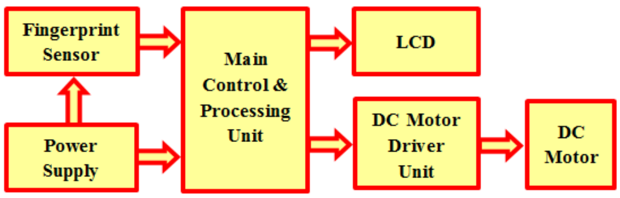

Figure 1. Block diagram of the motor control system

2.1. Fingerprint Sensor

A fingerprint scanner is a type of biometric scanner which scans the human fingerprint. There are many types of fingerprint sensor types, but most commonly used are optical fingerprint sensors and capacitive fingerprint sensors. Capacitive sensors use an array capacitor plates to image the fingerprint. Skin is conductive enough to provide a capacitive coupling with an individual capacitive element on the array. Capacitive sensors use a difference between skin-sensor and air-sensor contact in terms of capacitive values. When a finger is placed on the sensor, an array of pixels measures the variation in capacity between the valleys and the ridges in the fingerprint. Optical sensors use arrays of photodiode or phototransistor detectors to convert the energy in light incident on the detector into electrical charge. The sensor package usually includes a light emitting diode (LED) to illuminate the finger. With optical sensors, the finger is placed on a plate and illuminated by LED light sources. Through a prism and a system of lenses, the image is projected on a CMOS image sensor. Using frame grabber techniques, the image is stored and ready for analysis, as in [2].

The block diagram fingerprint sensor is shown in Figure 2. A sensor reads the ridge pattern on the finger surface and converts the analog reading in the digital form through an analog to digital (A/D) converter. An interface module is responsible for communicating (sending images, receiving commands, etc.) with external devices (personal computer), as in [3]. The cross section of fingerprint sensor is shown in Figure 3. The block diagram of fingerprint process system is shown in Figure 4. The photographs of capacitive fingerprint sensor and optical fingerprint sensor are shown in Figure 5 and Figure 6 respectively.

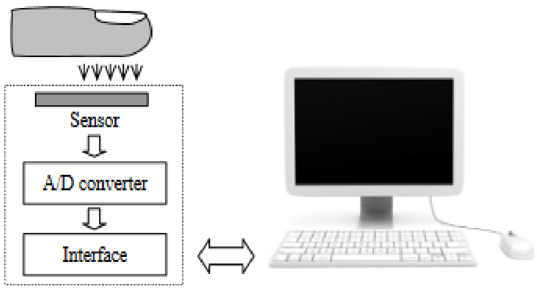

Figure 2. Block diagram of fingerprint sensor [3]

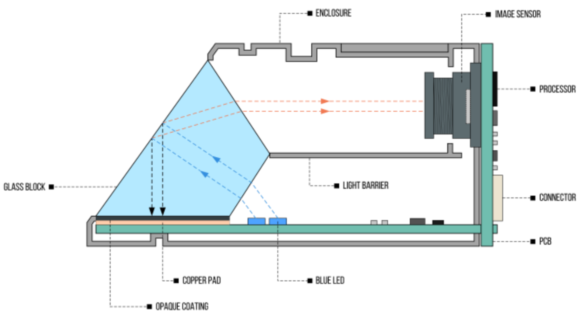

Figure 3. Cross section of fingerprint sensor [4]

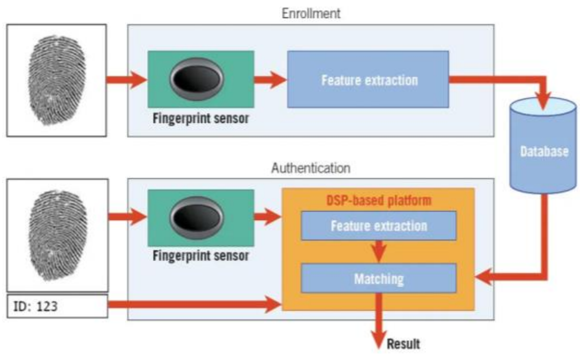

Figure 4. Block diagram of fingerprint process system [5]

Figure 5. Photograph of capacitive fingerprint sensor [6]

Figure 6. Photograph of optical fingerprint sensor [7]

In this work, an AS608 optical fingerprint sensor is used. This fingerprint sensor simplifies the process of fingerprint detection, storage, and verification. Inside the sensor is a high power digital signal processor (DSP) chip that does all image rendering, calculation, feature finding, and searching, as in [8]. The fingerprint scanner is frequently implemented in control access system. The reason being is because every human have different fingerprint minutiae which helps in identifying the true data of a person accurately. The AS608 fingerprint sensor is capable of storing up to 128 individual fingerprints. It is widely used by electronics business, information security, access control, identity authentication and other security industry. The photograph of fingerprint sensors is shown in Figure 7.

(a) Front view

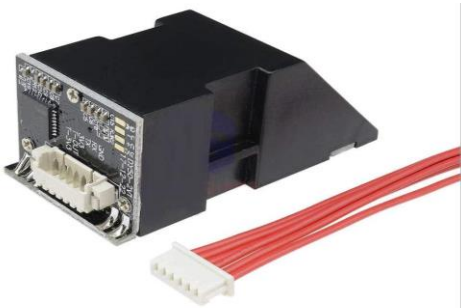

(b) Back view

Figure 7(a) and (b). Photograph of fingerprint sensor [8]

2.2. Alphanumeric LCD Display

The alphanumeric (A/N) LCD module can display characters, numerals, symbols and some limited graphics. The LCD module used in this research work is 2 lines and 16 characters matrix modules with light emitting diode (LED) back-lighting. Most LCD modules conform to a standard interface specification. A 2 x 16 LCD means it can display 16 characters per line and there are 2 such lines. In this LCD, each character is displayed in 5 x 7 pixel matrix. A 14-pin access having eight data lines, three control lines and three power lines is provided, as in [9]. Pin layout and photograph of the 2 × 16 LCD module are shown in Figure 8 and Figure 9.

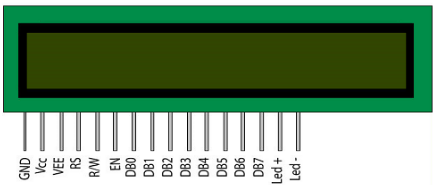

Figure 8. Pin layout of 2 × 16 LCD module

Figure 9. Photograph of 2 × 16 LCD module

2.3. ATMEGA328P Microcontroller

The Atmel Pico Power ATMEGA328P is a low-power Complementary Metal Oxide Semiconductor (CMOS) 8-bit microcontroller based on the Advanced Virtual RISC (AVR) enhanced Reduced Instruction Set Computing (RISC) architecture. By executing powerful instructions in a single clock cycle, the ATMEGA328P achieves throughputs close to one Million Instructions Per Second (1MIPS) per MHz. This empowers system designed to optimize the device for power consumption versus processing speed. The pin driver is strong enough to drive LED displays directly. All port pins have individually selectable pull-up resistors with a supply voltage invariant resistance. The device operates between 1.8 V to 5.5 V, as in [10]. The pin diagram and the photograph of ATMEGA328P microcontroller are shown in Figure 10 and Figure 11.

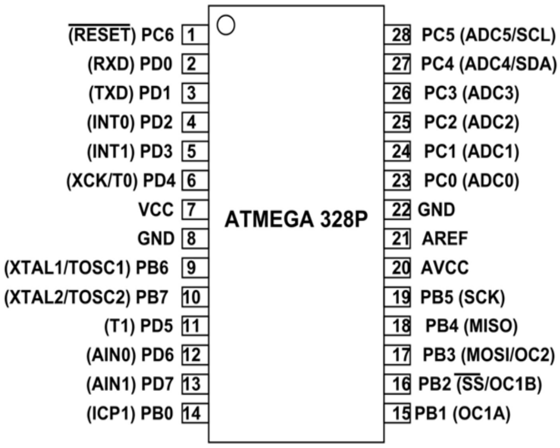

Figure 10. Pin diagram of ATMEGA328P microcontroller

Figure 11. Photograph of ATMEGA328P microcontroller

2.4. DC-DC Converter Module

DC-DC converter module is a power supply converter, and can perform 24-hour work do not need to strengthen heat. This is a dual output power module for various application using 5 V and 3.3 V and it is driven by DC 12 V input through two power integrated circuits to switch 5 V and 3.3 V. Pin assignments for P2, P3 and P4 are:

(a) P2 is 12 V input port: 12V 12V GND GND
(b) P3 is 12 V output port: GND GND ADJ SW 12V 12V

(c) P4 are 5 V & 3.3 V output port:
ADJ SW GND GND GND GND 5V 5V 3.3V 3.3V, as in [11].

The photograph of DC-DC converter module is shown in Figure 12.

Figure 12. Photograph of DC-DC converter module [11]

3. System Development

In the fingerprint section, AS608 fingerprint sensor is used to perform the process of fingerprint detection, storage, and verification. To perform these functions, AS608 fingerprint sensor is interfaced with ATMEGA328P microcontroller. Four connection pins of fingerprint sensor are Vcc, Tx, Rx and Gnd. In circuit connection, Vcc pin is applied +3.3 V and Gnd pin is directly grounded. For interfacing between AS608 fingerprint sensor and ATMEGA328P microcontroller, Tx and Rx of fingerprint sensor are connected to PD2 and PD3 of microcontroller respectively. Therefore, PD2 of microcontroller is used as digital input and PD3 of microcontroller is used as digital output. This sensor can store up to 128 fingerprint IDs, and therefore 128 different people can be enrolled into the system to open the door. After finishing fingerprint sensor circuit connection, the fingerprint enrolling code is uploaded into the ATMEGA328P microcontroller to register fingerprints.

The motor driver circuit is constructed by using two BC547 NPN transistors, two relays, protection diodes, and 5 V DC motor. In circuit connection, PD7 of ATMEGA328P microcontroller is connected to the base of BC547 transistor by inserting 1 kΩ resistor. The emitter is directly grounded and the collector is connected to one terminal of power supply of relay RLY1. Another terminal of power supply of RLY1 is applied +5 V, and a protection diode is also fitted at the relay's supply in the reverse direction. One input of relay is applied +5 V, and another input of relay is grounded. The connection of relay RLY2 is similar to that of RLY1 and it is controlled by PD8 of ATMEGA328P microcontroller. The two common poles of relays are fed to the terminals of DC motor.

In display circuit, VSS pin of LCD is connected to the ground and VCC pin is applied +5 V. The contrast control pin of LCD is connected to the voltage divider output of 5 kΩ variable resistor. In connection of voltage divider circuit, the first pin of variable resistor is applied +5 V, the second pin is voltage divider output and the third pin of variable resistor is connected to the ground. The contrast of LCD character can be controlled by turning variable resistor. Register select (RS) and enable (E) pins of LCD are controlled by PB5 and PB4 of ATMEGA328P microcontroller respectively. Read/Write (RW) pin of LCD is directly grounded. The interfacing between ATMEGA328P microcontroller and LCD is performed by using four bits mode. Therefore, DB4, DB5, DB6 and DB7 of LCD are connected to PB3, PB2, PB1 and PB0 of microcontroller respectively. The LCD back light pins such as LED+ and LED- are applied +5 V.

In power supply circuit, a 12 V battery is used as the built-in power source of the whole system. A DC-DC converter module is used to obtain the output voltages of 3.3 V, 5 V and 12 V. The negative terminal of the battery is connected to the GND pin of input line of DC-DC converter. The positive terminal the battery is connected to the Vin pin of input line of DC-DC converter by inserting "POWER" switch. The schematic diagram and photograph of the whole system are shown in Figure 13 and Figure 14.

In the software section, the source code for ATMEGA328P microcontroller is written using C programming language. Firstly, the digital input/output pins of microcontroller are configured for Tx and Rx of fingerprint sensor, LCD, and DC motor driver circuit. In this work, Adafruit Fingerprint sensor library, SoftwareSerial library and LiquidCrystal library are used to develop the complete code. After completing the code, it is compiled by using Arduino 1.8.12 software. The flow diagram of control program is shown in Figure 15.

In system operation, when the system power is switched-on, the LCD will show the message "Place Finger". When someone places a finger on the fingerprint sensor, and a match fingerprint is found, the motor will rotate in the clockwise direction to open the door. At the same time, the LCD will show the message "Allowed, Door Open". After ten seconds delay, the motor will rotate in the anticlockwise direction to close the door. If the fingerprint is no match, the system will not take any action at all and the LCD shows the message "No match fingerprint". The photographs of testing the developed system are shown in Figure 16.

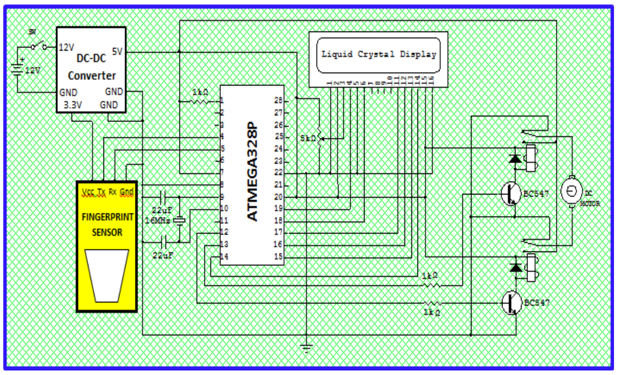

Figure 13. Schematic diagram of the whole system

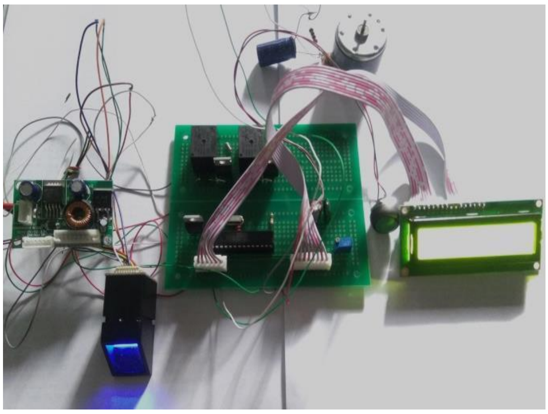

Figure 14. Photograph of the whole system

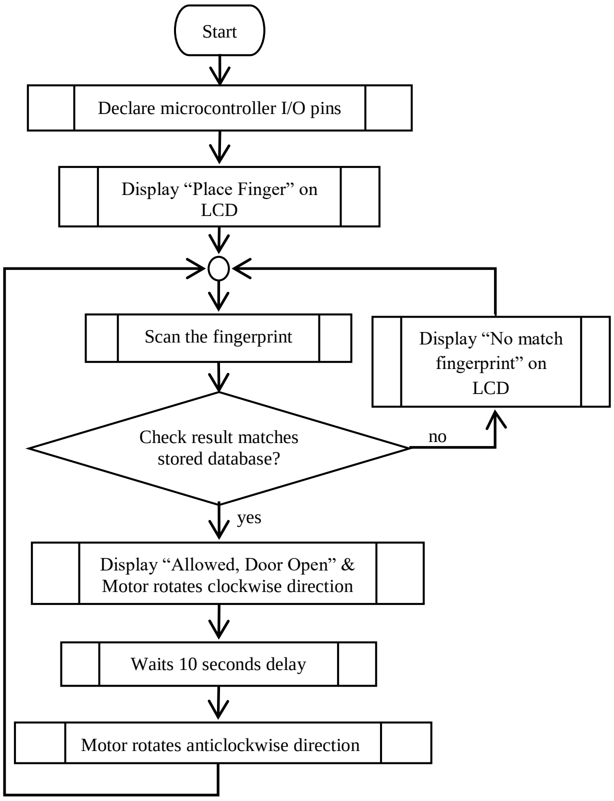

Figure 15. Flow diagram of control program

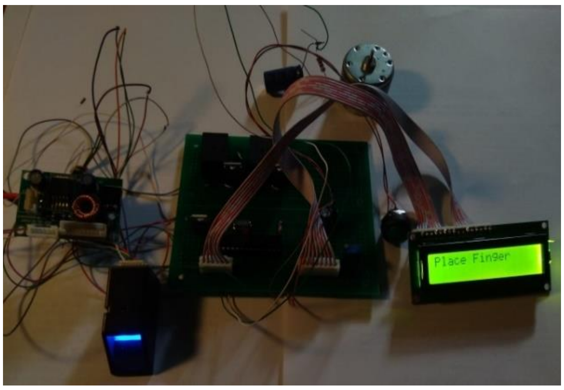

(a)

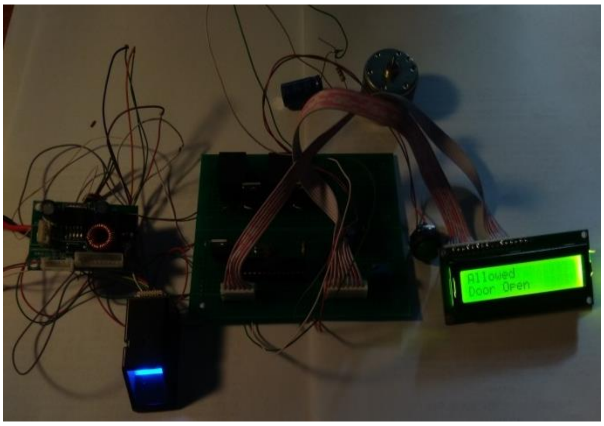

(b)

Figure 16 (a) and (b). Photographs of testing the constructed system

4. Discussion

The main goal of this research is to develop a motor control system using fingerprint sensor. In normal cases, the fingerprint sensor is able to detect the enrolled fingerprints. But, the performance of the fingerprint sensor is incorrect when the finger was muddy or oily condition. The time duration for scanning the fingerprint is 3 seconds. In this research, the developed system is only the performance of the motor rotation as clockwise and anticlockwise directions. The clockwise rotation of motor performs to open the door, and anticlockwise rotation of motor performs to close the door. The time duration of motor rotation can be varied by modifying control program. Two relays are used to control motor rotation. The relays used in this research are Single Pole Double Throw (SPDT) sealed relays. The relay's coil is rated up to 12 V, with a minimum switching voltage of 5 V. The fingerprint sensor used in this research is capable of storing up to 128 individual fingerprints. A 12 V battery is used as the built-in power source of the whole system. The operating voltage of the fingerprint sensor is 3.3 V and that of remaining circuit is 5 V. The power consumption of the whole system is 2.4 watts in motor rotation, and 1.3 watts in stand-by condition. There are some limitations in the developed system such as:

(a) The cost of the whole system can be a barrier to implementation.
(b) People who have suffered the loss of fingers, and their fingers may get rough which can lead to a miss-reading.
(c) System power error can take place wrong operation.
(d) If the peoples do not place their correct fingers in the right sensor pad, the fingerprint sensor may not read their identification correctly.

Table 1. Specification of the system

Microcontroller type	ATMEGA328P
External Input/ Power supply:	12 V, 4 A
DC-DC converter	5 V, 3.3 V, 2 A
Operation voltage and current	5 V, 0.5 A
Sensor type	Optical fingerprint sensor
Sensor window area	14 mm x 18 mm
Fingerprint imaging time	< 1.0 seconds
Sensor peak current	150 mA max
Sensor Signature file	256 bytes
Sensor Template file	512 bytes
LCD display	2-line 16-character LCD
Motor type (V and I)	DC motor (5 V, 250 mA)
Relay type (V and I)	Single Pole Double Throw (5 V, 70 mA)
Direction	Both forward and reverse
Motor speed	6000 rpm
Motor driver unit (V and I)	5 V, 70.5 mA
Power Consumption	2.4 W
Battery	12 V

5. CONCLUSIONS

In this research, a whole system has been designed, constructed and tested successfully. The whole system is constructed using modern electronic components such as fingerprint sensor, ATMEGA328P microcontroller, LCD, relays, DC motor, and other required components. By using servo motor or solenoid door lock, the constructed system can be applied in every home, office, school and university. Because of using fingerprint based circuit, the security of homes can also be improved because fingerprint duplication is not impossible. The developed system can also control larger power DC motor without changing the hardware design. To perform this condition, high current DC voltage must be applied to the input of the two relay, and the output of the two relay drives the larger power DC motor. By using this frame work, the biometric systems such as security systems, time attendance systems, door locks, physical access control systems, visitor identification systems, and biometric voter registration systems can also be implemented. To apply the developed system, the battery and circuit board should be placed in the room. The motor should be fitted at the door by using pulley or pinion. The fingerprint sensor and LCD should be fitted near the door entry at the height of 3 feet.

ACKNOWLEDGEMENTS

We are deeply thankful to Dr Win Swe, Acting Rector, Shwebo University for his kind permission to undertake this research.

We would like to extend our gratitude to Dr Min Swe, Professor and Head, Department of Physics, Shwebo University, and Dr Khin Hnin Ei, Professor, Department of Physics, Shwebo University, for their discussions, reviewing and approving to complete this research work.

REFERENCES

[1] D. Maio, D. Maltoni, R. Cappelli, J. L. Wayman, and A. K. Jain. “Fingerprint Verification Competition”, Proceedings of International Conference on Pattern Recognition (ICPR), Quebec City, Canada, 2002, pp.744-747.
[2] https://buysnip.com/fingerprint-sensor-types
[3] https://link.springer.com/chapter/10.1007/978-1-84882-254-2_2
[4] https://www.vishnumaiea.in/projects/hardware/interfacing-r307-optical-fingerprint-scanneer-with-arduino
[5] https://semiengineering.com/fingerprint-senor-technology-and-security requirements
[6] https://grow1.en.ec21.com/GROW_R300_Semiconductor_Capacitive_Fingerprint--10321654_10323663.html
[7] https://buysnip.com/product/r305-fingerprint-module/
[8] https://store.roboticsbd.com/sensors/1243-fingerprint-scanner-sensor-jm-101-robotics-bangladesh.html.
[9] J. Ilett, “How to Use Intelligent L.C.D.s”, Wimbrone Publishing Ltd, New York, 1997.
[10] Atmel Corporation, “ATmega328/P 8-bit AVR Microcontrollers Datasheet”, USA, 2016.
[11] https://www.prodctodc.com/benq-dc-12v-to-5v-33v-led-power-supply-regulator-step-down-converter-p-51.htm

Study on Neutron-Proton Scattering using CD-Bonn Potential

Thandar Kyi[1], Htun Htun Oo[2]
[1]*Lecturer, Dr, Department of Physics, Meiktila University, Meiktila, Myanmar*
[2]*Associate Professor, Dr, Department of Physics, Meiktila University, Meiktila, Myanmar*

ABSTRACT: *The neutron-proton scattering is studied by using CD-Bonn potential. Lippmann-Schwinger equation in momentum space is solved for two-body scattering process. Two-body transition matrix (T-matrix) is deduced and solved by numerical method. From that the scattering matrix (S) and their parameters such as phase shift (δ), mixing parameter (ε), scattering length (a) and effective range (r) are studied. The phase shifts (δ) and mixing parameters (ε) for neutron-proton scattering below the energy 350 MeV are studied. Low energy scattering parameters such as scattering length (a) and effective range (r) are studied for energy range from 0.001 MeV to 0.02 MeV. Our results of scattering length and effective range for single channel are* a_{np} *= - 23.7313 fm and* r_{np} *= 2.670 fm. Our results are good in agreement with experimental results,* a_{np}*= - (23.740 ± 0.020) fm and* r_{np} *= (2.77 ± 0.05) fm [1], [2], [3].*

Keywords: CD-Bonn potential, Lippmann-Schwinger equation, Numerical method, Scattering parameters

1. INTRODUCTION

The simplest system to investigate the forces which act between nucleons is the two-nucleon system. Many-body forces have not been studied in detail, because of the mathematical complexity in handling them. Indeed, much progress has been made in understanding features of nuclear behavior in terms of two-body forces. The two-body interactions are, of course, the proton-proton, neutron-neutron, neutron-proton interactions. A considerable amount of data is available on the scattering of a proton by a proton or neutron. Such data have been compiled for incident proton energy, ranging from a few MeV to a few hundred MeV. Especially, we studied neutron-proton scattering. The low energy scattering of the neutron-proton system is determined by two quantities: scattering length "a" and effective range "r" [4].

In this research we will present the very simple and easiest way to handle numerical technique for the two-body scattering problems. To study this two-body scattering system, the Lippmann-Schwinger equation is solved. In our two body Lippmann-Schwinger equation, CD-Bonn potential is used. The charge dependence (CD) predicted by the Bonn full model is reproduced accurately by the new potential, which is why we call the CD-Bonn potential [5]. But we will not discuss about this CD-Bonn potential in detail.

2. TWO-BODY SCATTERING SYSTEM

In studying the two-body system in momentum space, p we will apply Lippmann-Schwinger equation in ket form.

$$|\psi\rangle = \frac{1}{E-\hat{H}_0}\,\hat{V}\,|\psi\rangle \tag{1}$$

where, ψ is wave function, $\hat{H}_0$ is the kinetic energy operator and $\hat{V}$ is the potential energy operator. These will be singularity when the value of H_0 becomes close to E. To avoid the singularity of the operator, energy E is made to be slightly complex value. We can write the solution of Eq. (1) as

$$\left|\psi^{(+)}\right\rangle = |\psi_0\rangle + \frac{1}{E+i\varepsilon-\hat{H}_0}\,\hat{V}\left|\psi^{(+)}\right\rangle \tag{2}$$

where, $\left(\hat{H}_0 - E\right)|\psi_0\rangle = 0$. The state $\left|\psi^{(+)}\right\rangle$ is the scattering state for an outgoing wave in momentum space generated by the potential operator V. The $i\varepsilon$ is the correct boundary condition for an outgoing wave and $|\psi_0\rangle$ is the free momentum state which initiates the scattering process.

Let $|\psi_0\rangle = |p_0\rangle$ and $\left|\psi^{(+)}\right\rangle = \left|\psi^{(+)}_{p_0}\right\rangle$. By taking the inner product of Eq. (2) with the bra $|p\rangle$, we get

$$\left\langle p\middle|\psi^{(+)}_{p_0}\right\rangle = \langle p|p_0\rangle + \left\langle p\right|\frac{\hat{V}}{E+i\varepsilon-\hat{H}_0}\left|\psi^{(+)}_{p_0}\right\rangle \tag{3}$$

By operation of $\hat{H}_0$ on the bra $|p\rangle$, we can express the equation in simple form.

$$\psi^{(+)}_{p_0}(p) = \delta(p-p_0) + \frac{1}{E+i\varepsilon-\frac{p^2}{2\mu}}\left\langle p\right|\hat{V}\left|\psi^{(+)}_{p_0}\right\rangle \tag{4}$$

where, $\left\langle p\middle|\psi^{(+)}_{p_0}\right\rangle = \psi^{(+)}_{p_0}(p)$ and $\langle p|p_0\rangle = \delta(p-p_0)$. We insert the completeness relation $\int dp'\,|p'\rangle\langle p'| = 1$ into the above equation and becomes

$$\psi^{(+)}_{p_0}(p) = \delta(p-p_0) + \frac{1}{E+i\varepsilon-\frac{p^2}{2\mu}}\int dp'\,\langle p|\,\hat{V}\,|p'\rangle\psi^{(+)}_{p_0}(p') \tag{5}$$

The above equation contains the driving term in the form of a delta function and the pole term. It cannot be put directly into computer. So we need to define a new quantity called transition matrix (T-matrix) as

$$\left\langle p\right|\hat{V}\left|\psi^{(+)}_{p_0}\right\rangle = T(p,p_0) \tag{6}$$

We rewrite the Eq. (3) by inserting the operator $\hat{V}$ into both sides and the completeness relation into the right hand side of it. Then we get the following equation as

$$\left\langle p\right|\hat{V}\left|\psi^{(+)}_{p_0}\right\rangle = \langle p|\,\hat{V}\,|p_0\rangle +$$

$$\int dp' \langle p|\hat{V}|p'\rangle \frac{1}{E+i\varepsilon-\frac{p'^2}{2\mu}} \langle p'|\hat{V}|\psi_{p_0}^{(+)}\rangle \quad (7)$$

With the help of Eq. (6), we can write as

$$T(p,p_0) = V(p,p_0) + \int dp' V(p,p') \frac{1}{E+i\varepsilon-\frac{p'^2}{2\mu}} T(p',p_0) \quad (8)$$

where, $T(p,p_0)$ is transition matrix (T-matrix), which interprets as the transition from the initial momentum p_0 to the final momentum p because of the driving term $V(p,p_0)$. Therefore, T-matrix elements play an important role because which carry physical information.

2.1. T-matrix Element in Momentum Space

In this section, we will discuss the two body T-matrix elements. For the potential scattering, the Lipmann-Schwinger equation for T-matrix in operator form is

$$\hat{T} = \hat{V} + \hat{V} G_0 \hat{T} \quad (9)$$

In the above equation, G_0 is a free propagator and is defined by $G_0 = \frac{1}{E_0-\frac{\hat{p}^2}{2\mu}}$.

We consider the potential is spherically symmetric and $\ell = 0$. We need to project onto momentum space as follows

$$\langle p|\hat{T}|p'\rangle = \langle p|\hat{V}|p'\rangle + \langle p|\hat{V} G_0 \hat{T}|p'\rangle \quad (10)$$

We take the completeness relation onto the second part of the Eq. (10), then

$$\langle p|\hat{T}|p'\rangle = \langle p|\hat{V}|p'\rangle + \int p''^2 dp'' \langle p|\hat{V} G_0|p''\rangle\langle p''|\hat{T}|p'\rangle \quad (11)$$

By operation of G_0 on $|p''\rangle$, we get

$$\langle p|\hat{T}|p'\rangle = \langle p|\hat{V}|p'\rangle + \int p''^2 dp'' \frac{1}{E_0-\frac{p''^2}{2\mu}} \langle p|\hat{V}|p''\rangle\langle p''|\hat{T}|p'\rangle \quad (12)$$

Since, the incident energy, $E_0 = \frac{{p_0}^2}{2\mu}$, the Eq. (12) becomes

$$\langle p|\hat{T}|p'\rangle = \langle p|\hat{V}|p'\rangle + 2\mu \int p''^2 dp'' \frac{1}{p_0^2-p''^2} \langle p|\hat{V}|p''\rangle\langle p''|\hat{T}|p'\rangle \quad (13)$$

It can encounter the situation, $p_0 = p''$, then the integral will diverge and so we add iε to overcome this divergence.

$$\langle p|\hat{T}|p'\rangle = \langle p|\hat{V}|p'\rangle + 2\mu \int p''^2 dp'' \frac{1}{p_0^2+i\varepsilon-p''^2} \langle p|\hat{V}|p''\rangle\langle p''|\hat{T}|p'\rangle \quad (14)$$

We emphasize the second part of Eq. (14) and adding and subtracting the additional term

$$2\mu \int dp'' \frac{p_0^2}{p_0^2+i\varepsilon-p''^2} \langle p|\hat{V}|p_0\rangle\langle p_0|\hat{T}|p_0\rangle$$

and regroup this equation. And then we apply the principal value theorem, which is defined as

$$\lim_{\varepsilon\to 0} \frac{q}{x'+i\varepsilon} = \frac{q}{x'} - i\pi\delta(x')$$

Then we use the property of delta function $\delta(x^2-a^2) = \frac{1}{2|a|}[\delta(x+a)+\delta(x-a)]$ and the standard integration form, $\int_0^\infty \frac{1}{x^2-a^2}dx = \frac{1}{2a}\ln\frac{x-a}{x+a}$. We can get as

$$\langle p|\hat{T}|p'\rangle = \langle p|\hat{V}|p'\rangle + 2\mu \int dp'' \frac{p''^2 \langle p|\hat{V}|p''\rangle\langle p''|\hat{T}|p'\rangle - p_0^2\langle p|\hat{V}|p_0\rangle\langle p_0|\hat{T}|p_0\rangle}{p_0^2-p''^2} + \mu p_0 \langle p|\hat{V}|p_0\rangle\langle p_0|\hat{T}|p_0\rangle \left[\ln\left|\frac{p_0+p_{max}}{p_{max}-p_0}\right| - i\pi\right] \quad (15)$$

Our integral limit is from zero to infinity but we determine that p_{max} is enough for that limit. For $p' = p_0$, the Eq. (15) is

$$\langle p|\hat{T}|p_0\rangle = \langle p|\hat{V}|p_0\rangle + 2\mu \int dp'' \frac{p''^2 \langle p|\hat{V}|p''\rangle\langle p''|\hat{T}|p_0\rangle - p_0^2\langle p|\hat{V}|p_0\rangle\langle p_0|\hat{T}|p_0\rangle}{p_0^2-p''^2} + \mu p_0 \langle p|\hat{V}|p_0\rangle\langle p_0|\hat{T}|p_0\rangle \left[\ln\left|\frac{p_0+p_{max}}{p_{max}-p_0}\right| - i\pi\right] \quad (16)$$

The T-matrix element for on-shell is

$$\langle p_0|\hat{T}|p_0\rangle = \langle p_0|\hat{V}|p_0\rangle + 2\mu \int dp'' \frac{p''^2 \langle p_0|\hat{V}|p''\rangle\langle p''|\hat{T}|p_0\rangle - p_0^2\langle p_0|\hat{V}|p_0\rangle\langle p_0|\hat{T}|p_0\rangle}{p_0^2-p''^2} + \mu p_0 \langle p_0|\hat{V}|p_0\rangle\langle p_0|\hat{T}|p_0\rangle \left[\ln\left|\frac{p_0+p_{max}}{p_{max}-p_0}\right| - i\pi\right] \quad (17)$$

The above equation is integral form of T matrix elements and here we use the following notation.

$$\langle p|V|p'\rangle = V(p,p')$$

$$\langle p|T|p'\rangle = T(p,p')$$

To write the FORTRAN 90 code we need to transform T matrix elements in discrete form generally as,

$$T(p_i,p_0) = V(p_i,p_0) + 2\mu \sum_j w_j \frac{p_j^2 V(p_i,p_j)T(p_j,p_0) - p_0^2 V(p_i,p_0)T(p_0,p_0)}{p_0^2-p_j^2} + \mu p_0 V(p_i,p_0)T(p_0,p_0)\left[\ln\left|\frac{p_0+p_{max}}{p_{max}-p_0}\right| - i\pi\right] \quad (18)$$

We arrange as follows

$$T(p_i,p_0) = V(p_i,p_0) + 2\mu \sum_j w_j \frac{p_j^2 V(p_i,p_j)T(p_j,p_0)}{p_0^2-p_j^2} - 2\mu \sum_j w_j \frac{p_0^2 V(p_i,p_0)T(p_0,p_0)}{p_0^2-p_j^2} + \mu p_0 V(p_i,p_0)T(p_0,p_0)\left[\ln\left|\frac{p_0+p_{max}}{p_{max}-p_0}\right| - i\pi\right] \quad (19)$$

We simplify that

$$\widetilde{W}_j = \frac{2\mu w_j}{p_0^2-p_j^2} \quad (20)$$

$$C_i = \mu p_0 V(p_i,p_0)\left[\ln\left|\frac{p_0+p_{max}}{p_{max}-p_0}\right| - i\pi\right] \quad (21)$$

$$T_i = V_i + \sum_{j=1} \widetilde{W}_j p_j^2 V_{ij} T_j + \left(C_i - \sum_{j=1} \widetilde{W}_j p_0^2 V_i\right) T_0 \quad (22)$$

$$\tilde{C}_i = \left(C_i - \sum_{j=1} \widetilde{W}_j p_0^2 V_i\right) \quad (23)$$

The final equation in the compact form for fixed p_0 is

$$T_i = V_i + \sum_{j=1} \widetilde{W}_j\, p_j^2 V_{ij} T_j + \tilde{C}_i T_0 \quad (24)$$

This equation has a form that can be directly put into a computer. We can write down for the specific case; i = 0 to 2 and j = 1 to 2.

In the matrix form

$$\begin{bmatrix} \tilde{C}_0 - 1 & \widetilde{W}_1 p_1^2 V_{01} & \widetilde{W}_2 p_2^2 V_{02} \\ \tilde{C}_1 & (\widetilde{W}_1 p_1^2 V_{11} - 1) & \widetilde{W}_2 p_2^2 V_{12} \\ \tilde{C}_2 & \widetilde{W}_1 p_1^2 V_{21} & (\widetilde{W}_2 p_2^2 V_{22} - 1) \end{bmatrix} \begin{bmatrix} T_0 \\ T_1 \\ T_2 \end{bmatrix} = \begin{bmatrix} -V_0 \\ -V_1 \\ -V_2 \end{bmatrix}$$

$$[A][T] = [B]\,,\ \sum_{j=1} A_{ij} T_{ij} = B_j \quad (25)$$

The defined notations for A_{ij} matrix are

$$A_{ij} = \tilde{C}_{i-j} - \delta_{ij} \ \text{ for } (j = 1)$$

$$A_{ij} = \widetilde{W}_{j-1} p_{j-1}^2 V_{(i-1)(j-1)} - \delta_{ij} \ \text{ for } (j > 1)$$

$B_i = -V(p_{(i-1)}, p_0)$, where i =1, 2, 3,..., n.

Now, we have prepared the two-body T matrix equation for single channel complete enough to write the FORTRAN 90 code. This equation can be solved by using the Gauss Elimination Method.

For coupled channel we project Eq. (9) on partial wave state in momentum space. Then we get

$$\langle p\alpha|\, \hat{t}\, |p'\alpha'\rangle = \langle p\alpha|\, \hat{V}\, |p'\alpha'\rangle + \langle p\alpha|\hat{V} G_0\, \hat{t}\, |p'\alpha'\rangle \quad (26)$$

where, $\alpha = \{(\ell s) jmtm_t\}$ and then we can write

$$\langle p'(\ell' s') jmtm_t | t(E) | p(\ell s) jmtm_t\rangle = t_{\ell\ell'}^{sjtm_t}(p'p)\delta_{ss'}\delta_{jj'}\delta_{tt'}$$

$$\langle p'(\ell' s') jmtm_t | V | p(\ell s) jmtm_t\rangle = V_{\ell\ell'}^{sjtm_t}(p'p)\delta_{ss'}\delta_{jj'}\delta_{tt'}$$

Total spin ‘s’, total angular momentum ‘j’, total isospin ‘t’ and the 3rd component of isospin ‘m_t’ are conserved. So we can write $t_{\ell\ell'}^{sjtm_t} = t_{\ell\ell'}$. By applying completeness relation, Eq. (26) becomes

$$t_{\ell\ell'}(p, p') = V_{\ell\ell'}(p, p') + \sum_{\ell''} \int p''^2 dp'' \frac{2\mu}{p_0^2 - p''^2 + i\varepsilon} V_{\ell\ell'}(p, p'') t_{\ell''\ell'}(p'', p') \quad (27)$$

For $p' = p_0$,

$$t_{\ell\ell'}(p, p_0) = V_{\ell\ell'}(p, p_0) + \sum_{\ell''} \int p''^2 dp'' \frac{2\mu}{p_0^2 - p''^2 + i\varepsilon} V_{\ell\ell'}(p, p'') t_{\ell''\ell'}(p'', p_0) \quad (28)$$

We solved Eq. (28) in similar way as in single channel with the principal value theorem and it becomes

$$\begin{aligned} t_{\ell\ell'}(p, p_0) &= V_{\ell\ell'}(p, p_0) + 2\mu \sum_{\ell''} \int dp'' \frac{p''^2}{p_0^2 - p''^2} V_{\ell\ell''}(p, p'') t_{\ell''\ell'}(p'', p_0) \\ &\quad - 2\mu \sum_{\ell''} \int dp'' \frac{p_0^2}{p_0^2 - p''^2} V_{\ell\ell''}(p, p_0) t_{\ell''\ell'}(p_0, p_0) \\ &\quad + \mu p_0 \sum_{\ell''} \left[\ln\left|\frac{p_0 + p_{max}}{p_{max} - p_0}\right| - i\pi\right] V_{\ell\ell''}(p, p_0) t_{\ell''\ell'}(p_0, p_0) \end{aligned} \quad (29)$$

We transform the above equation into discrete form to write FORTRAN-90 code and we get as

$$t_{\ell\ell'}(p_i, p_0) - \sum_{\ell''} \sum_{p_j} K_{\ell\ell''}(p_i, p_j)\, t_{\ell''\ell'}(p_j, p_0) - \sum \tilde{C}_{\ell\ell''}(p_i, p_0)\, t_{\ell''\ell'}(p_0, p_0) = V_{\ell\ell''}(p_i, p_0) \quad (30)$$

where, $K_{\ell\ell''}(p_i, p_j) = \widetilde{w}_j p_j^2 V_{\ell\ell''}(p_i, p_j)$

$$\widetilde{w}_j = \frac{2\mu w_j}{p_0^2 - p_j^2}$$

$$C_{\ell\ell''}(p_i, p_0) = \mu p_0 \left[\ln\left|\frac{p_0 + p_{max}}{p_{max} - p_0}\right| - i\pi\right] V_{\ell\ell''}(p_j, p_0)$$

$$\tilde{C}_{\ell\ell''}(p_i, p_0) = \sum_{\ell''}\left\{C_{\ell\ell''}(p_i, p_0) - \sum_j \widetilde{w}_j\, p_0^2 V_{\ell\ell''}(p_i, p_0)\right\}$$

In the compact form, the final equation for fixed p_0 is

$$t_{\ell\ell'}(p_i) - \sum_{\ell''} \sum_{p_j} K_{\ell\ell''}(p_i, p_j)\, t_{\ell''\ell'}(p_j) - \sum \tilde{C}_{\ell\ell''}(p_i)\, t_{\ell''\ell'}(p_0) = V_{\ell\ell''}(p_i) \quad (31)$$

where, ℓ, ℓ', ℓ''=0, 2 and i, j=1, 2, 3,….., N.

2.2. Scattering Matrix and Scattering Parameters

The scattering matrix called S-matrix relates the initial state and the final state of a physical system undergoing a scattering process. More formally, the S-matrix is defined as the unitary matrix connecting asymptotic particle states in the Hilbert space of physical states (scattering channels). The relation between S-matrix and T-matrix in uncoupled (single) channel is

$$S = 1 - 2i\mu\pi p_0 t(p_0, p_0) \quad (32)$$

where, $\mu =$ reduced mass of particles, $p_0 =$ initial momentum. In the scattering process, the phase of the outgoing wave is changed by an additional phase factor $e^{2i\delta}$ due to the potential effect.

In the uncoupled case, the phase shift and S-matrix are calculated by using the following equations. The properties of symmetry and unitarily reduce the number of parameters necessary to parameterize the S-matrix elements. As a consequence the complex number $S_{\ell\ell'}$ can be parameterized by one real number, the phase $\delta_{\ell\ell'}$.

$$S_{\ell\ell'} = \exp(2i\delta_{\ell\ell'}) \quad (33)$$

$$\delta = \frac{1}{2}\tan^{-1}\left(\frac{\mathrm{Imag}(S)}{\mathrm{Real}(S)}\right) \quad (34)$$

For coupled case, the S-matrix is 2×2 matrix. The uncoupled elements are again parameterized by one real phase, whereas the unitary and symmetric 2×2 matrix needs 3 parameters. The S-matrix will have the structure

$$S = \begin{pmatrix} S_{11} & S_{12} \\ S_{21} & S_{22} \end{pmatrix} \quad (35)$$

One can show that $S = S^{\dagger}$, symmetric such as $S_{12} = S_{21}$. We get three unitarily relations as follow.

$$S_{11}S_{11}^* + S_{12}S_{12}^* = 1 \quad (36)$$

$$S_{11}S_{21}^* + S_{12}S_{22}^* = 1 \quad (37)$$

$$S_{21}S_{21}^* + S_{22}S_{22}^* = 1 \quad (38)$$

Therefore, three conditions, three parameters characterize the unitary 2×2 matrix.

$$S_{11} = |S_{11}|e^{2i\delta_{11}},\ S_{12} = |S_{12}|e^{2i\delta_{12}},\ S_{22} = |S_{22}|e^{2i\delta_{22}} \quad (39)$$

Since $|S_{11}|^2 + |S_{12}|^2 = 1$, we can choose as

$$|S_{11}| = \cos 2\varepsilon,\ |S_{12}| = \sin 2\varepsilon,\ |S_{22}| = \cos 2\varepsilon \quad (40)$$

Then we will substitute Eq. (39) and Eq. (40) into Eq. (37)

$$e^{2i(\delta_{11}-\delta_{12})} + e^{2i(\delta_{12}-\delta_{22})} = 0$$

$$e^{2i(\delta_{11}+\delta_{22})} = -e^{4i\delta_{12}} \text{ or } e^{2i\delta_{12}} = ie^{i(\delta_{11}+\delta_{22})} \quad (41)$$

By using the Eq.(39) and Eq.(41), the S-matrix becomes

$$S = \begin{pmatrix} \cos 2\varepsilon\, e^{2i\delta_1} & i \sin 2\varepsilon\, e^{i(\delta_1+\delta_2)} \\ i \sin 2\varepsilon\, e^{i(\delta_1+\delta_2)} & \cos 2\varepsilon\, e^{2i\delta_2} \end{pmatrix}$$

This is called the “Stapp” phase shift parameterization.

The connections between the S-matrix and T-matrix are

$$S_{11} = 1 - 2i\mu\pi p_0 t_{11},\ S_{12} = -2i\mu\pi p_0 t_{12}$$

$$S_{21} = -2i\mu\pi p_0 t_{21},\ S_{22} = 1 - 2i\mu\pi p_0 t_{22} \quad (42)$$

The phase shift (δ) for coupled case is

$$\delta_1 = \frac{1}{2}\tan^{-1}\left(\frac{\mathrm{Imag}(S_{11})}{\mathrm{Real}(S_{11})}\right),$$

$$\delta_2 = \frac{1}{2}\tan^{-1}\left(\frac{\mathrm{Imag}(S_{22})}{\mathrm{Real}(S_{22})}\right) \quad (43)$$

In addition to the phase shifts the asymptotic scattering for coupled states is characterized by a coupling parameter ε, which indicates the strength of the tensor force. The parameter ε, induced by the tensor force, couples the states $^3S_1$ and $^3D_1$ and plays an important quantitative role for the binding energy of nuclei. It gives a measure of the effect of the tensor potential between the neutron and the proton. This tensor potential is important for the existence of the only bound state of the neutron-proton system, the deuteron.

The mixing parameter can be calculated, using the following equation.

$$\varepsilon = \frac{1}{2}\tan^{-1}\left[i^{(\ell-\ell')}\left(-i\frac{S_{12}}{S_{11}}\, e^{i(\delta_1-\delta_2)}\right)\right] \quad (44)$$

From phase shift result, we can evaluate the effective range and scattering length by using the following equation.

$$p\cot\delta = -\frac{1}{a} + \frac{1}{2}rp^2 + \cdots \quad (45)$$

where, ‘a’ is the scattering length and ‘r’ is the effective range.

3. Results And Discussion

The n-p scattering process is studied for single and coupled channels with the help of FORTRAN-90. We continue to some discussion on the phase shifts and mixing parameters of p-n interaction for isospin, T=1 and isospin, T=0. Therefore, we need to define the integral range in momentum space p of Eq. (29) in FORTRAN code as that ($p_0 = 0\ fm^{-1}$, $p_{mid} = 10\ fm^{-1}$, $p_{max} = 35\ fm^{-1}$, Np = 28) which give the numerical stability of T-matrix.

We will calculate the phase shifts (δ) and the mixing parameters (ε) for n-p scattering below incident energy in the laboratory frame, E_{Lab}=350 MeV.

For isospin, T=1 and the total angular momentum $J_{max} \leq 4$, the corresponding partial wave states ($^{2S+1}L_J$) are $^1S_0$, $^3P_0$, $^3P_1$, $^1D_2$, $^3P_2$, $^3F_2$, ε_2, $^3F_3$, $^1G_4$, $^3F_4$, $^3H_4$, ε_4. The variation of phase shifts and mixing parameters of the partial wave states for isospin, T=1 and total angular momentum ($0 \leq J \leq 2$) with incident energy are shown in Table 1 and Figure 1. The variation of phase shifts and mixing parameters of the partial wave states for isospin, T=1 and total angular momentum ($3 \leq J \leq 4$) with incident energy are shown in Table 2 and Figure 2.

For isospin, T=0 and the total angular momentum $J_{max} \leq 4$ the corresponding partial wave states are $^1P_1$, $^3S_1$, $^3D_1$, ε_1, $^3D_2$, $^1F_3$, $^3D_3$, $^3G_3$, ε_3, $^3G_4$. The variation of phase shifts and mixing parameters of the partial wave states for isospin, T=0 and total angular momentum ($1 \leq J \leq 2$) with incident energy are shown in Table 3 and Figure 3. The variation of phase shifts and mixing parameters of the partial wave states for isospin, T=0 and total angular momentum ($3 \leq J \leq 4$) with incident energy are shown in Table 4 and Figure 4.

The phase shift (δ) depends on both potential and scattering energy. Negative phase shifts indicate a repulsive potential and positive phase shifts indicate an attractive potential. This indicates the relation between the sign of the phase shift and the behavior of the potential.

In studying n-p scattering, at lower energies the attractive part of the potential has the predominant effect and the $^1S_0$ phase shift is positive. In particular, the $^1S_0$ phase shift is positive till 250 MeV but this is negative from 300 MeV. So, at high energies the $^1S_0$-waves feel the repulsive core while the $^1D_2$, $^3D_2$ and $^3D_3$ waves do not.

Table 1. The n-p phase shifts for isospin, T=1 and total angular momentum, 0 ≤ J ≤ 2.

E_{lab} (MeV)	$^1S_0$	$^3P_0$	$^3P_1$	$^1D_2$	$^3P_2$	$^3F_2$	ε_2
1	62.09	0.18	-0.11	0.00	0.02	0.00	0.00
5	63.66	1.61	-0.93	0.04	0.26	0.00	-0.05
10	59.99	3.63	-2.04	0.16	0.72	0.01	-0.18
25	50.91	8.11	-4.82	0.69	2.60	0.09	-0.76
50	40.43	10.74	-8.19	1.73	5.94	0.30	-1.64
100	26.35	8.56	-13.25	3.87	11.02	0.72	-2.63
150	16.28	3.70	-17.52	5.82	13.99	1.03	-2.90
200	8.27	-1.57	-21.40	7.46	15.67	1.19	-2.79
250	1.54	-6.71	-24.98	8.77	16.60	1.17	-2.50
300	-4.30	-11.58	-28.30	9.77	17.08	0.98	-2.12
350	-9.48	-16.14	-31.39	10.50	17.28	0.62	-1.72

Table 2. The n-p phase shifts for isospin, T=1 and total angular momentum, $3 \le J \le 4$.

Elab (MeV)	$^3F_3$	$^1G_4$	$^3F_4$	$^3H_4$	ε_4
1	0.00	0.00	0.00	0.00	0.00
5	0.00	0.00	0.00	0.00	0.00
10	-0.03	0.00	0.00	0.00	0.00
25	-0.20	0.03	0.02	0.00	-0.04
50	-0.62	0.13	0.11	0.02	-0.17
100	-1.42	0.39	0.48	0.09	-0.49
150	-1.98	0.67	1.01	0.20	-0.79
200	-2.33	0.96	1.59	0.31	-1.05
250	-2.51	1.26	2.15	0.43	-1.25
300	-2.57	1.56	2.65	0.54	-1.42
350	-2.53	1.85	3.07	0.64	-1.54

Table 3. The n-p phase shifts for isospin, T=0 and total angular momentum, $1 \le J \le 2$.

E_{lab} (MeV)	$^1P_1$	$^3S_1$	$^3D_1$	ε_1	$^3D_2$
1	-0.19	147.73	-0.01	0.11	0.01
5	-1.49	118.15	-0.18	0.68	0.22
10	-3.05	102.58	-0.68	1.17	0.85
25	-6.35	80.59	-2.81	1.81	3.73
50	-9.73	62.69	-6.45	2.13	8.98
100	-14.44	43.02	-12.27	2.45	17.24
150	-18.34	30.42	-16.51	2.79	22.10
200	-21.79	20.90	-19.70	3.19	24.52
250	-24.86	13.17	-22.13	3.60	25.36
300	-27.59	6.60	-24.04	4.00	25.21
350	-30.02	0.87	-25.55	4.38	24.44

Table 4. The n-p phase shifts for isospin, T=0 and total angular momentum, $3 \le J \le 4$.

E_{lab} (MeV)	$^1F_3$	$^3D_3$	$^3G_3$	ε_3	$^3G_4$
1	0.00	0.00	0.00	0.00	0.00
5	-0.01	0.00	0.00	0.01	0.00
10	-0.07	0.01	0.00	0.08	0.01
25	-0.42	0.05	-0.05	0.55	0.17
50	-1.11	0.33	-0.26	1.61	0.72
100	-2.15	1.45	-0.94	3.49	2.18
150	-2.87	2.71	-1.77	4.84	3.65
200	-3.48	3.70	-2.60	5.77	4.99
250	-4.09	4.31	-3.39	6.40	6.18
300	-4.74	4.54	-4.10	6.84	7.21
350	-5.45	4.44	-4.72	7.14	8.08

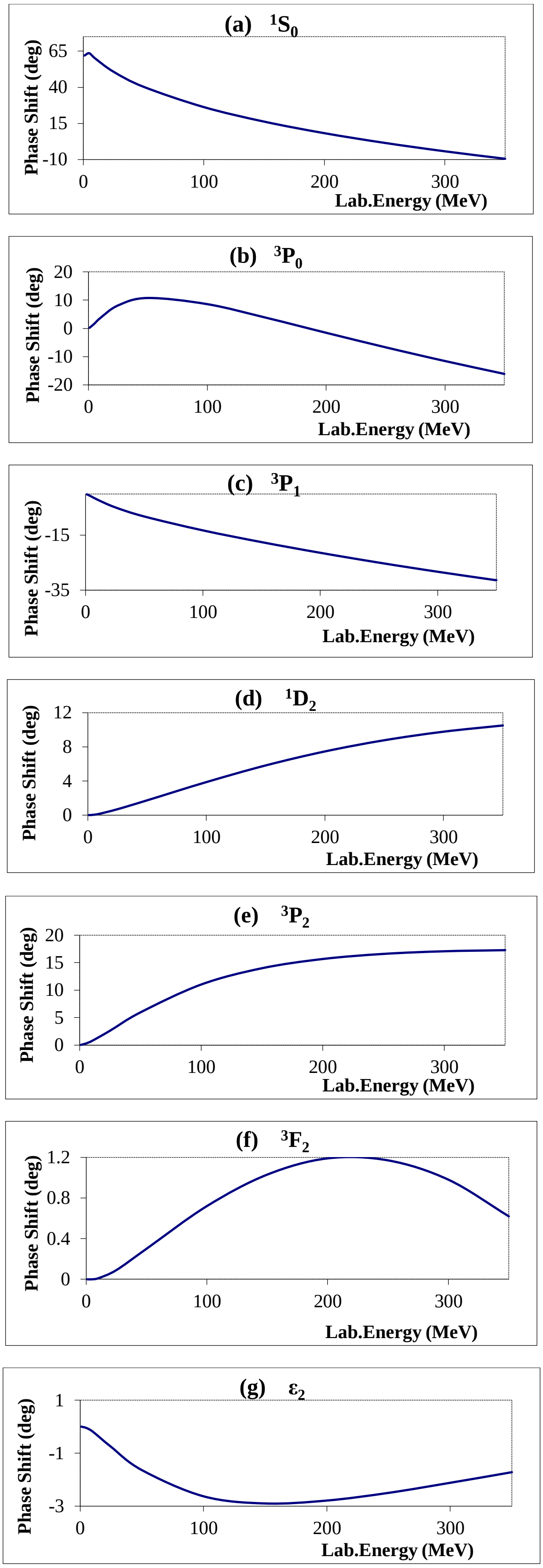

Figure 1. Variations of n-p phase shifts with incident energy for isospin, T=1 ($0 \le J \le 2$).

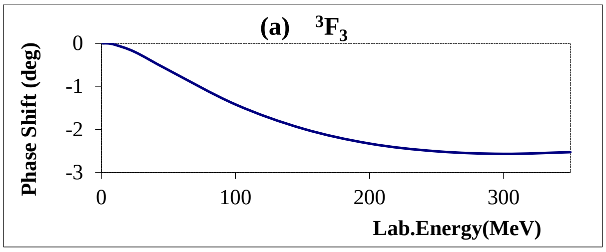

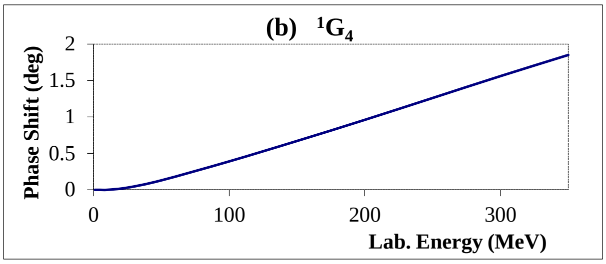

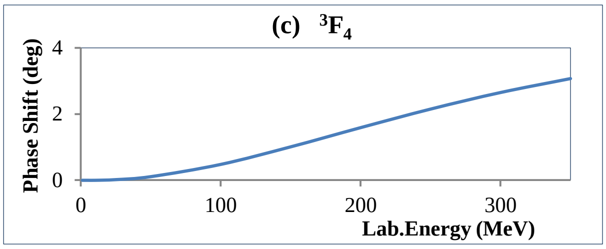

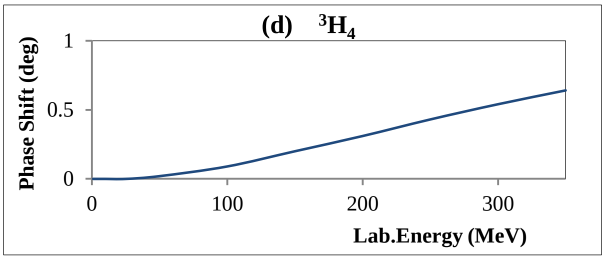

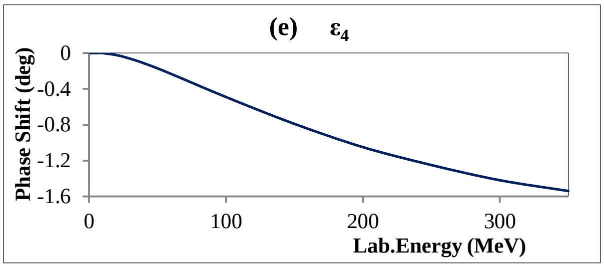

Figure 2. Variations of n-p phase shifts with incident energy for isospin, T=1 ($3 \le J \le 4$).

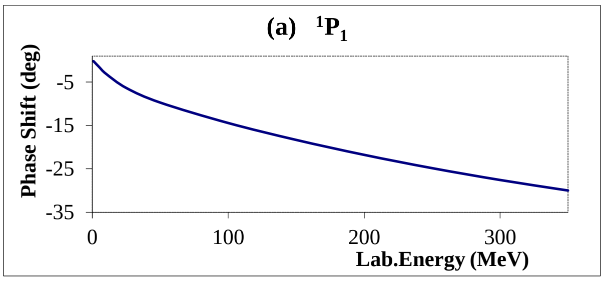

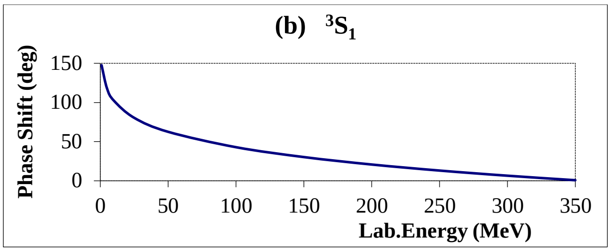

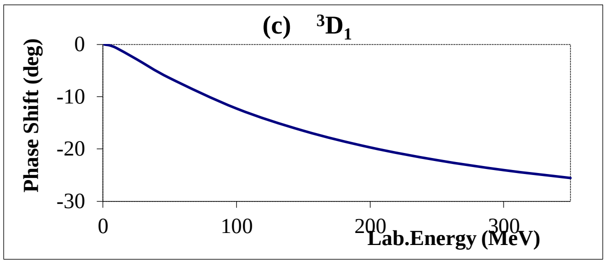

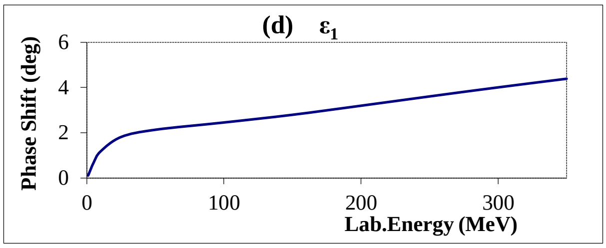

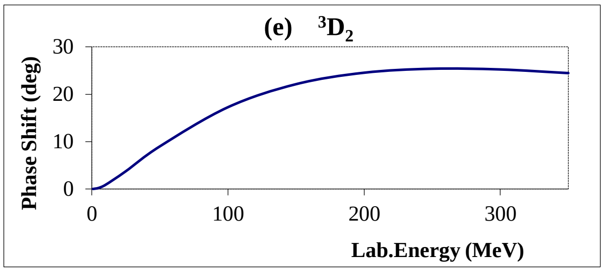

Figure 3. Variations of n-p phase shifts with incident energy for isospin, T=0 ($1 \le J \le 2$).

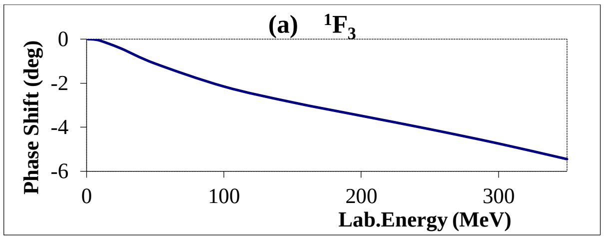

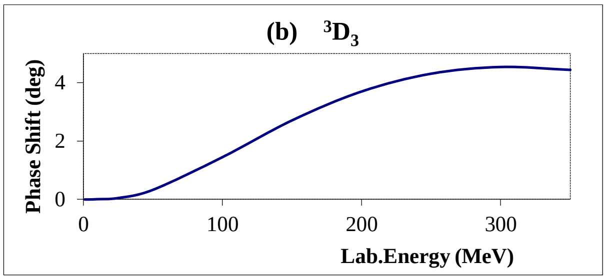

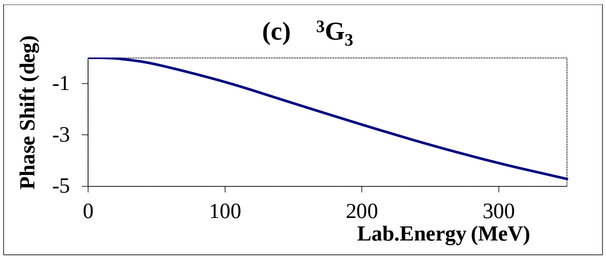

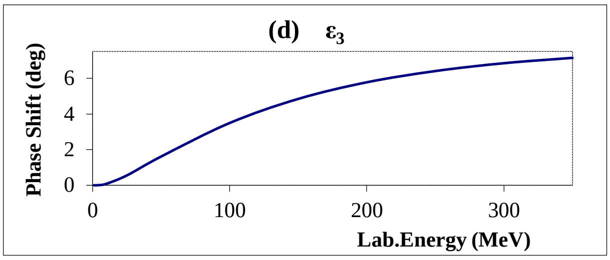

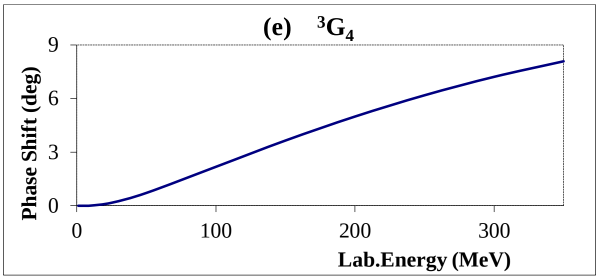

Figure 4. Variations of n-p phase shifts with incident energy for isospin, T=0 ($3 \le J \le 4$).

Table 5. Low energy scattering parameters for energy range from 0.01 MeV to 0.2 MeV.

E_{lab} (MeV)	Scattering length, a (fm)	Effective range, r (fm)
0.01	-23.731362	2.670258
0.04	-23.731292	2.669564
0.08	-23.731089	2.668648
0.12	-23.730767	2.667742
0.16	-23.730326	2.666848
0.20	-23.729771	2.665964

Table 6. Low energy scattering parameters for energy range from 0.001 MeV to 0.02 MeV.

E_{lab} (MeV)	Scattering length, a (fm)	Effective range, r (fm)
0.001	-23.731370	2.670572
0.004	-23.731369	2.670502
0.008	-23.731367	2.670409
0.012	-23.731364	2.670316
0.016	-23.731359	2.670223
0.020	-23.731354	2.670130

But when incident energy becomes higher, it can approach the interior part and it feels the repulsive interaction. The $^1S_0$ and $^3P_0$ phase shifts change from positive to negative at about 200 MeV.

At energies below 100 MeV, the largest phase shifts are the $^1S_0$-wave and $^3S_1$-wave phase shifts. Both $^1S_0$ and $^3S_1$ phase shifts are positive, while the $^1P_1$ and $^3P_1$ phase shifts are negative.

Finally, low energy scattering parameters such as scattering length (a) and effective range (r) are studied for single channel, $^1S_0$ as shown in Table 5 and Table 6.

4. Conclusion

A rough generalization is that the forces are attractive in even states, repulsive in odd states. Phase shifts and coupling parameters for higher partial waves are quite small. The mixing parameter ε_2, induced by the tensor force, couples the states $^3P_2$ and $^3F_2$. Similarly, the mixing parameter ε_4 couples the states $^3F_4$ and $^3H_4$. The mixing parameter ε_1, couples the states $^3S_1$ and $^3D_1$.

In studying low energy scattering parameters the energy must be less than 10MeV. The values of scattering length and effective range for $^1S_0$ state become converged to one decimal place in the energy range from 0.01 MeV to 0.2 MeV as shown in Table 5. Then energy range is changed to the range from 0.001 MeV to 0.02 MeV which gives the numerical stability for scattering length to four decimal places, a_{np} = - 23.7313 fm and effective range to three decimal places, r_{np} = 2.670 fm as shown in Table 6. Since the scattering length is negative, the potential is attractive but not enough attractive enough (the state is virtual) for $^1S_0$ state.

Acknowledgements

We would like to thank Professor Dr. Hla Hla Than, Head of Department of Physics, Meiktila University and Professor Dr. Daw Hla Win, Department of Physics, Meiktila University for their encouragement to do this research work.

In addition, grateful thanks are also to all teaching staff of Physics Department, Meiktila University.

References

[1] T. L. Houk, Phys. Rev. C 3, 1886 [1971]; W. Dilg, ibid. 11, 103 (1975).

[2] L. Koester and W. Nistler, Z. Phys. A 272, 189 (1975).

[3] S. Klarsfeld, J. Martorell, and D. W. L. Sprung, J. Phys. G 10, 165 (1984).

[4] M.A. Preston, "Phys of the Nucleus", Addison-Wesley Publishing Co, Inc, London) (1962).

[5] R. Machleidt, et al., (2001) Phys. Rev. C 63, 24001.

Characterization of Advanced Superionic Conducting Materials of Lithium Cobalt-Nickel Oxides for Solid Oxide Fuel Cell (SOFC) Application

Aye Aye Lwin[1], Win Kyaw[2], Thaik Thaik[3], San San Wai[4]
[1,2,3]Associate Professor, Department of Physics, Loikaw University
[4]Professor and Head, Department of Physics, Loikaw University
[1]ayeayelwin635@gmail.com, [2]wkyaw08@gmail.com, [3]homehider12345@gmail.com, [4]sansanwai1963@gmail.com

ABSTRACT: *Advanced superionic conductors (AdSICs) are key materials for developing solid-state batteries (SSBs) such as lithium ion battery. In this work, Lithium Cobalt-Nickel Oxides with the general formula $LiCo_{1-x}Ni_xO_2$ (where x = 0.00, 0.50 and 1.00) were prepared by conventional ceramic technique. The samples were characterized by X-ray diffraction (XRD) and Scanning Electron Microscopy (SEM) to confirm the crystalline phase formation and to examine the microstructural characteristics of the desired materials. XRD patterns indicated that the samples analogous to rhombohedral structure and the lattice parameters increased with increase in concentration of Ni. SEM micrographs showed that the spherical shape composed of small spherical grains and the grain sizes decreased with increase in concentration of Ni. The grain sizes were very fine particles nature of the samples. For the application of solid oxide fuel cell (SOFC) materials, electrical conductivities of the samples were investigated in the temperature range of 298 K – 883 K. It was found that the samples exhibited as the advanced superionic conductors (AdSICs).*

Keywords: $LiCo_{1-x}Ni_xO_2$; XRD; SEM; dc electrical conductivity; solid oxide fuel cell

1. INTRODUCTION

Research on solid state ionics (SSIs) materials is an interdisciplinary area of research for the Physicists, Material Scientists, Chemists, Engineers and Technologists. Solid state ionic conductors having the conductivity order of 10^{-11} to 10^{-3} S m^{-1} at ambient temperature are called normal ionic conductors (NICs) [1]. Some solid state ionic conductors have a high conductivity of the order of 10^{-3} S m^{-1} or more with negligible electronic conductivity of the order of about 10^{-9} S m^{-1} at room temperature as well as high temperature are called superionic conductors (SICs). Solid state ionic conductors are often called superionic conductors (SICs) or fast ionic conductors (FICs) or solid electrolytes (SEs) [2].

Superionic conductors (SICs) have been attracted considerably due to their potential applications in various electrochemical devices, such as, fuel cells, solid state batteries, sensors, timers, memories, capacitors, etc [3]. Superionic conductors where σ is more than 0.1 S cm^{-1} (i.e., $\sigma \geq 0.1$ S cm^{-1} at 300 K) and the activation energy for ion transport E_a is small (about $E_a \leq 0.1$ eV), are called advanced superionic conductors (AdSICs). These materials are useful in batteries and various sensors. Especially they are used primarily in solid oxide fuel cells (SOFCs). A solid oxide fuel cell is an electrochemical conversion device that produces electricity directly from oxidizing a fuel [4, 5]. Fuel cells are characterized by their electrolyte material; the SOFC has a solid oxide or ceramic electrolyte [6]. Most of the conventional ionic devices were made up of liquid electrolytes and these have many limitations like (i) short self-life time period and (ii) instability towards the temperature variations, etc. These limitations have initiated to search for new solids with high ionic conductivity [7]. The main attractive properties of superionic conducting materials are high ionic conductivity, wide range of operating temperature, stability, ruggedness, miniaturization, etc. [8]. Many superionic conducting materials are synthesized by various techniques such as solid state reactions, melt quench, sol-gel process, thermal evaporation, sputtering, etc., for different ionic device applications. Based on the microstructures, superionic conductors are classified as single or polycrystalline, amorphous or glassy, composites and polymers.

Due to the wide range of applications of the superionic conductors (SICs), in this work, superionic materials of Lithium Cobalt-Nickel Oxides, $LiCo_{1-x}Ni_xO_2$ (where x = 0.00, 0.50 and 1.00) were prepared and characterized by XRD and SEM. Furthermore, the temperature dependence of electrical conductivities and activation energies of the samples were investigated for the application of solid oxide fuel cell materials.

2. MATERIALS AND METHODS

2.1. Sample Preparation

Lithium Cobalt-Nickel Oxides, $LiCo_{1-x}Ni_xO_2$ (where x = 0.00, 0.50 and 1.00) were prepared by conventional ceramic technique using the starting materials of analytical reagent (AR) grade Lithium Hydroxide Monohydrate ($LiOH.H_2O$), Nickel Oxide (NiO) and Cobalt Oxide (CoO). These starting materials were weighed with desired stoichiometric compositions and mixed each other to be homogeneous. The mixed powder was ground by an agate mortar and pestle for 2 h to obtain fine powder of solid solution. The fine powder was inserted into the crucible and covered with mica-sheet. The crucible was placed in the JLabTech Electric Oven. The powders were heated at 450°C for 8 h and followed by 800°C for 15 h in JLabTech Electric Oven to be crystalline phase and cooled down to room temperature (25°C).

2.2. Materials Characterization

The crystalline phase formation, the crystal structure and the lattice parameters of the product materials of $LiCo_{1-x}Ni_xO_2$ (where x = 0.00, 0.50 and 1.00) were analyzed using an X-Ray Diffractometer (PC-controlled SHIMADZU XRD 6100, Japan) [University Research Centre (URC), University of Magway] employing CuK_α radiation $\lambda = 1.5406$ Å with a 2θ range of 20º – 70º and scan-speed of 4º per minute. Microstructural characteristics of the samples were examined using a Scanning Electron Microscope (SEM) (JCM-6000Plus, Japan) [Department of Geology, Taungoo University] with electrons accelerating voltage of 15 kV and 2000 times of photo magnification.

2.3. Electrical Property Measurement

For the investigation of electrical conductivity, the samples were performed circular shape pellets using hydraulic pellet-maker with 70 MPa. Thicknesses and areas of the samples were 6.0×10^{-3} m and 9.51×10^{-7} m^2 respectively. The electrical contacts on the specimens were facilitated by a silver paste between sample and copper electrodes. The electrical resistances were measured by Proskit MT-12330 digital multimeter between 298 K and 883 K with the step of 15 K in air using the two-probe parallel-plate capacitor method. In this measurement, DELTA A-Series DTA-4896 Temperature Controller was used as a temperature controlled element and K-type thermocouple was used to record real temperatures throughout the measurement. 300 W heater rods were used for heating elements.

3. Results And Discussion

3.1. Phase Identification and Structure Analysis

XRD patterns of as-prepared $LiCo_{1-x}Ni_xO_2$ (where x = 0.00, 0.50 and 1.00) samples are shown in Figure 1. It is clear that all the samples exhibit a layered hexagonal structure. Highly crystalline peaks are in good agreement with the Joint Committee on Powder Diffraction Standards (JCPDS) files of (i) Cat. No. 00-050-0653> $LiCoO_2$, Lithium Cobalt Oxide for x = 0.00 sample; (ii) Cat. No. 00-050-0653> $LiCoO_2$, Lithium Cobalt Oxide and Cat. No. 00-062-0468> $LiNiO_2$, Lithium Nickel Oxide for x = 0.50 sample; and (iii) Cat. No. 00-062-0468> $LiNiO_2$, Lithium Nickel Oxide for x = 1.00 sample. In the collected XRD patterns, there are no observable impurities phases.

The crystallite sizes D are estimated by using the Debye–Scherrer equation, $D = 0.9\lambda/\beta \cos\theta$, where λ is the wavelength of incident X-ray, β is the full width at half maximum (FWHM) and θ is the Bragg angle. Both the lattice parameters and crystallite sizes are tabulated in Table 1. The lattice parameters obtained in this work are almost agreed with the results of Yudha, C.S. et al. (2019) [9]. Variations of the lattice parameters with increase in Ni concentration are shown in Figure 2. It is clearly

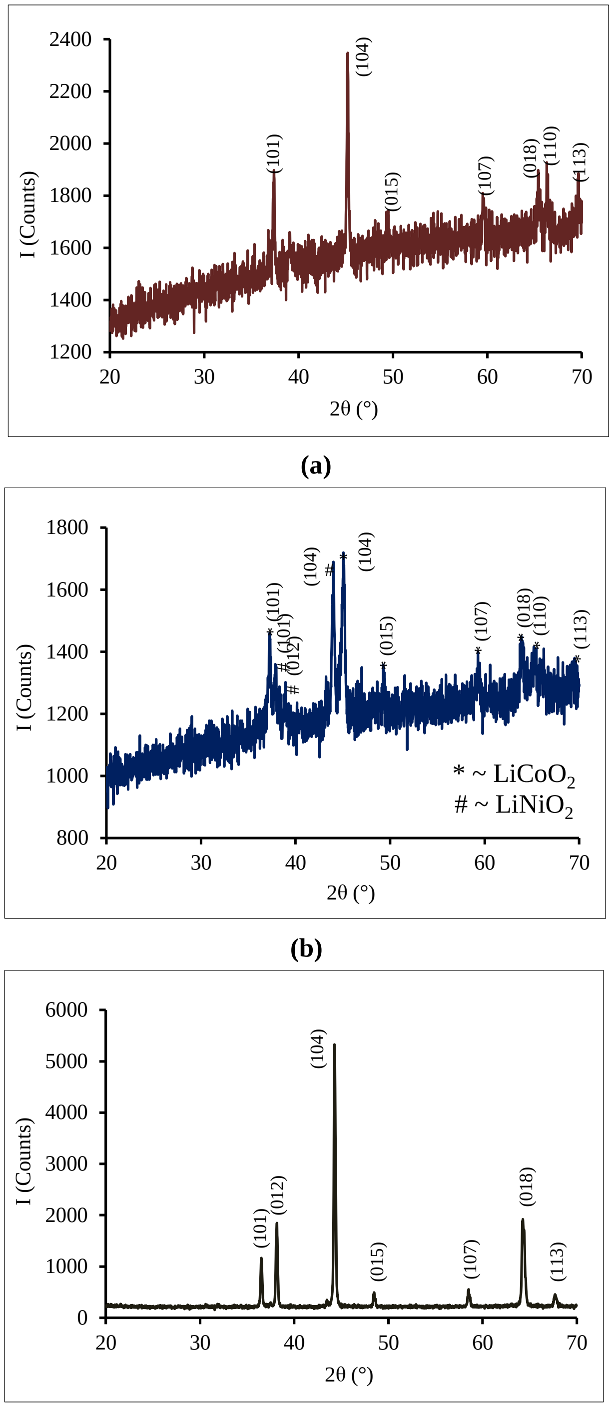

Figure 1. XRD patterns of $LiCo_{1-x}Ni_xO_2$ where (a) x = 0.00, (b) x = 0.50 and (c) x = 1.00 samples

Table 1. The lattice parameters and crystallite sizes of $LiCo_{1-x}Ni_xO_2$ (where x = 0.00, 0.50 and 1.00) samples

x	*a* = *b* (Å)	*c* (Å)	*D* (nm)
0.00	2.8150	14.0493	57.72
0.50	2.8519	14.1389	22.02
1.00	2.8799	14.1384	44.57

shown that the lattice parameters a and b increased with increase in Ni concentration. The c/a values decreased with increase in Ni concentration from 5.0085 to 4.9093,

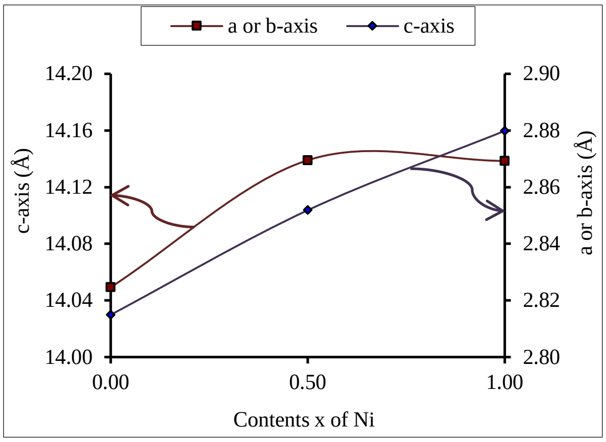

Figure 2. Variations of the lattice parameters with increase in Ni concentration of $LiCo_{1-x}Ni_xO_2$ samples

which, means that the sample exhibits a more ordered layered structure (or intercalation) in a hexagonal unit cell. The crystallite sizes are varied alternately.

3.2. Microstructural Analysis

Figure 3 shows the SEM micrographs of $LiCo_{1-x}Ni_xO_2$ (where x = 0.00, 0.50 and 1.00) samples. The images revealed that the grain shape of the samples were found to be spherical composed of very small spheres. Some pores appeared in the observed micrographs. The average grain sizes of the samples were evaluated by using Image J software and the obtained grain sizes were listed in Table 2. The grain size of the x = 0.50 is found to be the smallest one among the investigated samples. The grain sizes of the samples are submicron-sized particles. The grain sizes varied with increase in Ni concentration.

3.3. Superionic Conductivity Study

The temperature dependence of the electrical conductivity σ of a solid state ionic (SSI) material obeys an Arrhenius expression, $\sigma = \sigma_0 \exp(-E_a/kT)$, where σ_0 is the pre-exponential factor, E_a is the activation energy, k is the Boltzmann constant and T is absolute temperature. The Arrhenius plots of the electrical conductivity shows that the conduction in $LiCo_{1-x}Ni_xO_2$ (where x = 0.00, 0.50 and 1.00) samples is thermally activated owing to the semiconducting character of these oxides as shown in Figure 4. All observed phenomena for the electronic transport can be ascribed to small-polaron conduction.

Activation energy of the samples was determined by the slope of the linear plots drawn between log σ and 1000/T. The obtained activation energies with suitable temperature ranges of the samples are tabulated in the Table 3. The value of activation energy varies with the Ni composition increases from x = 0.00 to 1.00. The variation of activation energy may be occurred the number of oxygen vacancies in the sample due to thermal agitation. It may be also due to increase in conductivity with increase in Ni concentration.

The DC electrical conductivity is one of the useful experimental techniques to understand conductivity mechanism. The DC conductivity of the

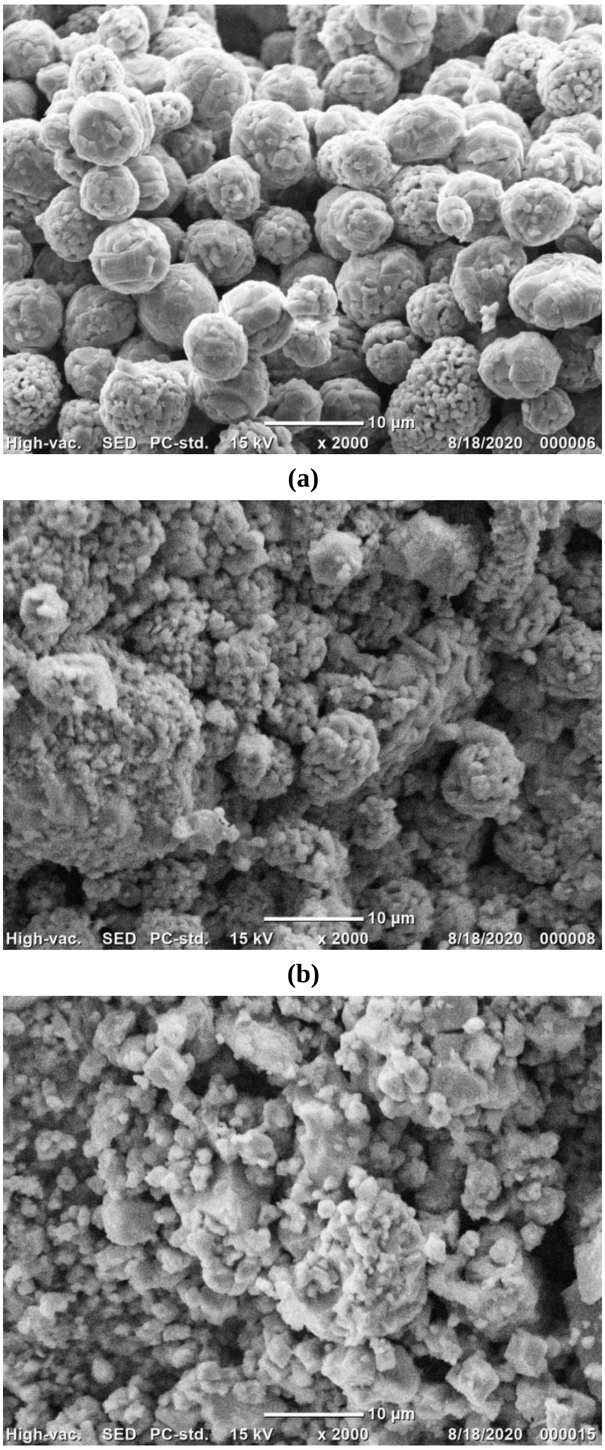

(a)

(b)

(c)

Figure 3. SEM micrographs of $LiCo_{1-x}Ni_xO_2$ where (a) x = 0.00, (b) x = 0.50 and (c) x = 1.00 samples

Table 2. The grain sizes of $LiCo_{1-x}Ni_xO_2$ (where x = 0.00, 0.50 and 1.00) samples

x	Grain sizes (µm)
0.00	0.0651
0.50	0.0149
1.00	0.0278

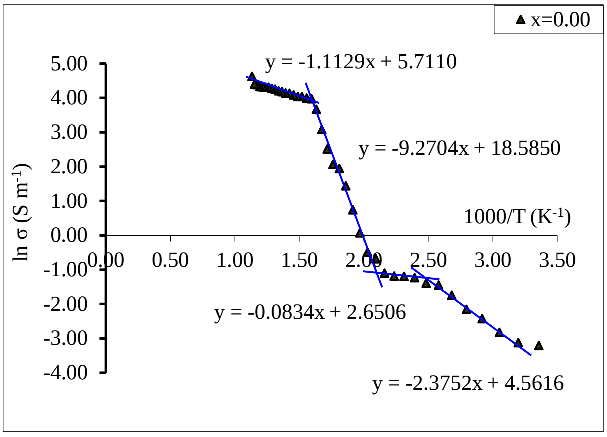

(a)

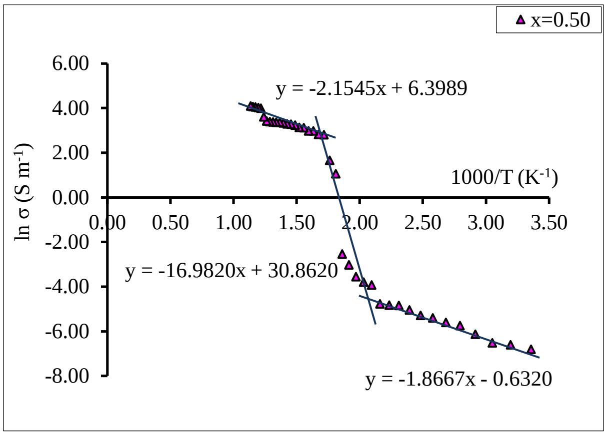

(b)

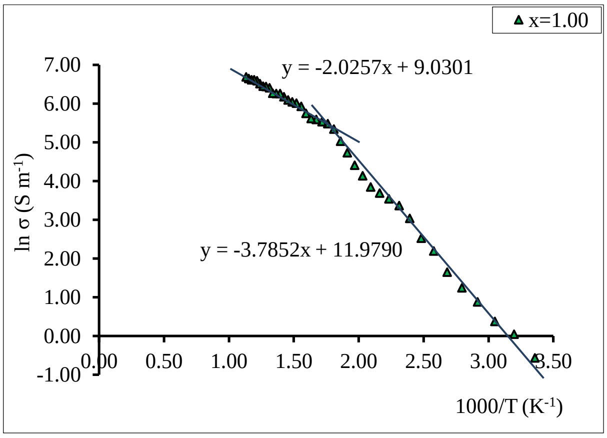

(c)

Figure 4. Arrhenius plots of the $LiCo_{1-x}Ni_xO_2$ where (a) x = 0.00, (b) x = 0.50 and (c) x = 1.00 samples

Table 3. Activation energies of $LiCo_{1-x}Ni_xO_2$ (where x = 0.00, 0.50 and 1.00) samples

x	Temperature range (K)	E_a (eV)
0.00	298 – 388	0.2049
	388 – 463	0.0072
	463 – 883	0.7996
0.50	298 – 463	0.0160
	463 – 583	0.9647
	583 – 883	0.1858
1.00	298 – 568	0.3265
	568 – 883	0.1747

samples is estimated by two probe method. Variations of the electrical conductivities of the samples are shown in Figure 5. Experimental results of the temperature dependence of electrical conductivities of the samples are listed in Table 4.The electrical conductivity of the $LiCo_{1-x}Ni_xO_2$ (where x = 1.00) is the highest one among the investigated samples. As presented in Figure 5, the electrical conductivities show that the samples exhibit the semiconductor nature in the temperature range of 298 K – 598 K. Experimental results of the temperature dependence of electrical conductivities of the samples are listed in Table 4.

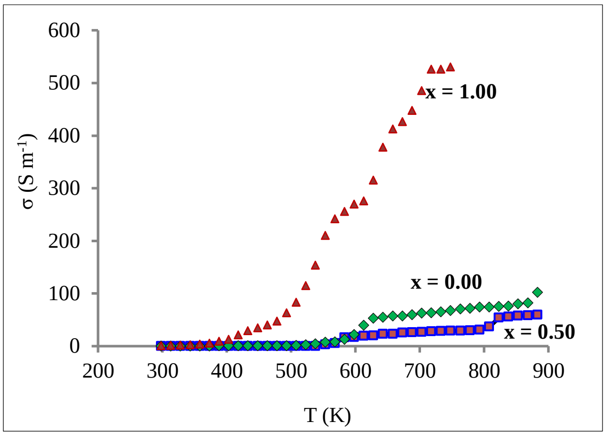

Figure 5. Comparison of the electrical conductivities with temperature of the $LiCo_{1-x}Ni_xO_2$ (where x = 0.00, 0.50 and 1.00) samples

As presented in Table 4, the obtained electrical conductivity σ values are greater than 1×10^{-3} S m^{-1} ($\sigma \geq 1\times10^{-3}$ S m^{-1}). It shows that the $LiCo_{1-x}Ni_xO_2$ (where x = 0.00, 0.50 and 1.00) samples exhibit as the superionic conductors (SICs). Furthermore, some of the obtained activation energies E_a listed in Table 3 are less than 0.1 eV ($E_a \leq 0.1$ eV). Therefore, the $LiCo_{1-x}Ni_xO_2$ (where x = 0.00 and 0.50) samples are advanced superionic conductors (AdSICs) because they are superionic conductors (SICs) with the activation energies in the temperature range of 388 K – 463 K for x = 0.00 sample and in the temperature range of 298 K – 463 K for x = 0.50 sample are less than 0.1 eV.

In our modern society, from cell phone to artificial heart and from electric vehicle to satellites, batteries have become an indispensable technology. Compared with the current batteries with liquid electrolytes, batteries with solid electrolytes hold the promise of greater safety, higher power, and higher energy densities. However, development of the all-solid-state batteries is limited by the relatively low conductivity of the solid electrolyte materials. Most families of the superionic conductors have activation energy in the range of 0.3 – 0.9 eV and exhibit ionic conductivities of the order of 10^{-3} – 10^{-1} S m^{-1} at room temperature (RT). Lithium superionic conductors with Li^+ conductivity that is comparable with that of the organic liquid electrolytes are critical for the development of practically useful all-solid-state batteries (ASSBs). Here, we show that the

Table 4. Experimental results of the temperature dependence of electrical conductivity of $LiCo_{1-x}Ni_xO_2$ (where x = 1.00, 0.50 and 1.00) samples

T(K)	x=0.00 σ (S m^{-1})	x=0.50 σ (S m^{-1})	x=1.00 σ (S m^{-1})
298	4.05E-02	1.10E-03	5.74E-01
313	4.41E-02	1.36E-03	1.05E+00
328	5.94E-02	1.48E-03	1.47E+00
343	8.86E-02	2.17E-03	2.43E+00
358	1.16E-01	3.20E-03	3.51E+00
373	1.75E-01	3.71E-03	5.26E+00
388	2.35E-01	4.51E-03	9.02E+00
403	2.48E-01	5.09E-03	1.26E+01
418	2.92E-01	6.44E-03	2.10E+01
433	3.03E-01	7.89E-03	2.94E+01
448	3.06E-01	7.99E-03	3.47E+01
463	3.32E-01	8.41E-03	4.02E+01
478	5.05E-01	1.97E-02	4.71E+01
493	6.13E-01	2.25E-02	6.31E+01
508	1.07E+00	2.87E-02	8.30E+01
523	2.10E+00	4.85E-02	1.15E+02
538	4.21E+00	7.89E-02	1.54E+02
553	7.01E+00	2.87E+00	2.10E+02
568	7.89E+00	5.26E+00	2.42E+02
583	1.24E+01	1.64E+01	2.56E+02
598	2.18E+01	1.68E+01	2.70E+02
613	3.92E+01	1.95E+01	2.76E+02
628	5.30E+01	1.97E+01	3.16E+02
643	5.44E+01	2.27E+01	3.78E+02
658	5.69E+01	2.29E+01	4.12E+02
673	5.69E+01	2.52E+01	4.26E+02
688	5.95E+01	2.63E+01	4.48E+02
703	6.25E+01	2.69E+01	4.85E+02
718	6.31E+01	2.79E+01	5.26E+02
733	6.51E+01	2.87E+01	5.26E+02
748	6.71E+01	2.89E+01	5.30E+02
763	7.01E+01	2.92E+01	6.13E+02
778	7.17E+01	2.98E+01	6.31E+02
793	7.42E+01	3.06E+01	6.37E+02
808	7.42E+01	3.67E+01	6.79E+02
823	7.51E+01	5.39E+01	7.34E+02
838	7.60E+01	5.58E+01	7.51E+02
853	7.99E+01	5.74E+01	7.51E+02
868	8.20E+01	5.84E+01	7.79E+02
883	1.02E+02	5.95E+01	8.09E+02

$LiCo_{1-x}Ni_xO_2$ samples can have very high conductivities of 10^{-3} to over 10^{-1} S m^{-1} at room temperature with low activation energy under 1 eV. Thus it can be suggested that the samples can be applied as solid oxide fuel cells (SOFCs) materials in all-solid-state batteries (ASSBs).

4. CONCLUSION

Solid state superionic (SSI) materials of Lithium Cobalt-Nickel Oxides, $LiCo_{1-x}Ni_xO_2$ (where x = 0.00, 0.50 and 1.00) were successfully prepared by conventional ceramic technique. From the XRD results, the samples were single phase hexagonal crystalline materials. Microstructural analysis proved that spherical grains composed of very small spheres were obtained. The grains sizes showed that the samples were sub-micro particles of fine powder. The main results of temperature dependence of electrical conductivity are that the DC conductivity increases as Ni content increases and it reach maxima. In the temperature range of 298 K – 598 K, they are semiconductor-like materials. The activation energy varied with different Ni compositions. The $LiCo_{1-x}Ni_xO_2$ (where x = 0.00, 0.50 and 1.00) samples are superionic conductors from 298 K to 883 K in which x = 0.00 and x = 0.50 samples are advanced superionic conductors (AdSICs) due to the lowest activation energies. According to experimental results, the samples can be applied as the solid oxide fuel cells (SOFCs) materials in rechargeable batteries. Furthermore, it can be promised that the x = 0.00 and x = 0.50 samples are more suitable for the applications of SOFCs materials among the investigated materials.

ACKNOWLEDGEMENT

The authors would like to acknowledge Prof. Dr. Htay Aung, Acting-Rector, Loikaw University, for his kind permission and valuable suggestions to do this work.

REFERENCES

[1] A. Andreeva, and A. Despotuli, “NEW GEOMETRY AND PROPERTIES OF ADVANCED SUPERIONIC CONDUCTORS”, Journal of Nanomaterials, 2019, Vol. 1, pp. 48-53.

[2] M. Aniya, “Understanding the mechanism of superionic transport from trends of materials properties”, Physics Procedia, 2013, Vol. 44, pp. 25-34.

[3] P. Kalyani, and N. Kalaiselvi, “Various aspects of $LiNiO_2$ chemistry: A review”, Science and Technology of Advanced Materials, 2005, Vol. 6, pp. 689-703.

[4] P.P. Kumar, and S. Yashonath, “Ionic conduction in the solid state”, Journal of Chemical Science, 2006, Vol. 118 (1), pp. 135-154.

[5] K. Siraj, “Past, Present and Future of Superionic Conductors”, International Journal of Nano and Material Sciences, 2012, Vol. 1 (1), pp. 1-20.

[6] H. Tao, Z. Feng, H. Liu, X. Kan, and P. Chen, “Reality and Future of Rechargeable Lithium Batteries”, The Open Materials Science Journal, 2011, Vol. 5 (2), pp. 204-214.

[7] G.T.K Fey, R.F. Shiu, T. P. Kumar, and C.L. Chen, “Preparation and characterization of lithium nickel cobalt oxide powders via a wet chemistry processing”, Materials Science and Engineering B100, 2003, pp. 234-243.

[8] N. Bensalah, and H. Dawood, “Review on Synthesis, Characterizations, and Electrochemical Properties of Cathode Materials for Lithium Ion Batteries”, Journal of Material Science & Engineering, 2016, Vol. 5 (4), pp. 1-21.

[9] C.S. Yudha, S.U. Muzayanha, H. Widiyandari, F. Iskandar, W. Sutopo, and A. Purwanto, “Synthesis of $LiNi_{0.85}Co_{0.14}Al_{0.01}O_2$ Cathode Material and its Performance in an NCA/Graphite Full-Battery”, Energies, 2019, Vol. 12, pp. 1-14.

Scanning System for Light Transmission of Glasses

Shwe Zin Aung
Professor and Head, Physics Department, Monywa University
shwezinaung@gmail.com

ABSTRACT: *Scanning system for light transmission through glasses and transparent materials was developed by using PIC 16F84A and PIC 18F452 microcontrollers. The system includes area scanning unit, data acquisition and signal processing unit. The homogeneity of the specific area of the glass sheet can be investigated by the aid of area scanning unit of the system. The maximum area of 7.5 cm×6.5 cm can be scanned and area investigated in each scan is 0.5 cm×0.5 cm which is limited by the size of the detector. In this device the eight different colors of LEDs are used as light sources and light transmission through the glass sheet is sensed by LDR. Both software and hardware were developed for two constructed units. A visual C#.Net program is also developed to display the scanning result as a color graph on the personal computer. The transmitted light intensity (LUX) and transmission percentage are displayed on LCD. It is also displayed graphically and numerically on the computer monitor. The system takes 6 min for one complete measurement. The system can be used as spectrophotometer in the field of chemical and medical analysis. The system can be modified and used in photo absorption measurement in material science.*

Keywords: scanning system; visual C#.Net program, PIC18F452; color map;

1. INTRODUCTION

Scanning system for light transmission measurement has been developed by using the microcontrollers. This project is intended to measure the amount of light transmission of the glass sheet. The system can measure the light transmission through the transparent material and it can check homogeneity of the specific area of the transparent materials. This measuring system is electro-mechanical device. It is an electronics controlled mechanical-movement for area scanning of the glass sample and analog signal processing. PIC16F84 microcontroller is used for controlling the motion of area scanning mechanism and PIC18F452 microcontroller is used for signal processing [3] and interfacing with personal computer.

2. MATERIALS AND METHOD

This present work uses PIC16F84A and PIC18F452 microcontrollers (µCs) as controls devices. PIC16F84A is used to control the area scanning mechanism and to send the acknowledge signal to the PIC18F452 µC. According to the acknowledge signal of PIC16F84A µC the analog signal from the sensors¸ light dependence resistor and phototransistor, are read by built in analog to digital converter (ADC) of the PIC 18F452 µC. Eight LEDs in different colors and a laser pointer are used as the light sources and LDR and phototransistor sense the light intensities from them.

3. DEVELOPMENT OF SYSTEM

Both hardware and software development were performed in this research. Construction of the microcontroller based scanning system for light transmission measurement composes of mechanical portion and electronic portion. The mechanism of area scanning was developed and is an essential part of the constructed system to measure the light transmission of the specific area of the glass sample.

The scanning mechanism hold the glass sample and move in the X direction step by step Then it moves in Y direction at the end of the X motion under the light beam. The lens track mechanism of DVD player is used for X motion and that of VCD player is used for Y motion. The maximum distance of X motion and Y motion are 7.5 cm and 6.5 cm respectively. So the maximum scanning area of scanning unit is (7.5cm×6.5cm) and (0.5cm×0.5cm) area is occupied for one scanning.

Electronic portion involves power supply unit, motor driver unit, microcontroller based motor control unit, transducer unit, the light source unit, signal processing unit and LCD display unit and interfacing with computer through parallel port of PC for displaying the measured result in color format on monitor. The complete circuit diagram for whole system is shown in Figure 1.

Software for PIC 16F84A and PIC18F452 and personal computer were developed. Each and every processor performs the specific task written in different level languages. Motor driving and motor controlling will make by PIC16F84A and MPLAB assembly program was developed. Built in ADC of PIC 18F452 reads the analog signal from transducer unit and converts it to digital form. The C programs in Mikroelektronika C compiler version 7.0.0.3 implements AD conversion, digital signal processing and sending this to PC, display the results on LCD. Interfacing with computer was also developed and reliable window programming C#.Net was used.

3.1 Motor Driver Unit

For measuring the transmission of light through the specified area of glass plate we have to scan the glass plate with the light beam. To perform the scanning, the glass plate will be moved in the X and Y direction by using the motors. To drive the X motor and Y motor in clockwise or counter clockwise direction, two "H bridge" motor driver circuits are constructed [2].

Port B (RB0 to RB3) of MCU 16F84A [6] are used as output ports and port A (RA0 to RA3) of MCU 16F84A are arranged as input ports. MCLR pin is applied as reset pin. Output port RB0 and RB1 produce the signal for X-motor driver circuit and output port RB2 and RB3 are used for Y-motor driver circuit. In each output line, four diodes (D1, D2, D3, and D4) are installed for protection the microcontroller from back current. The trigger pulse produced by microcontroller is too low to drive the motors.

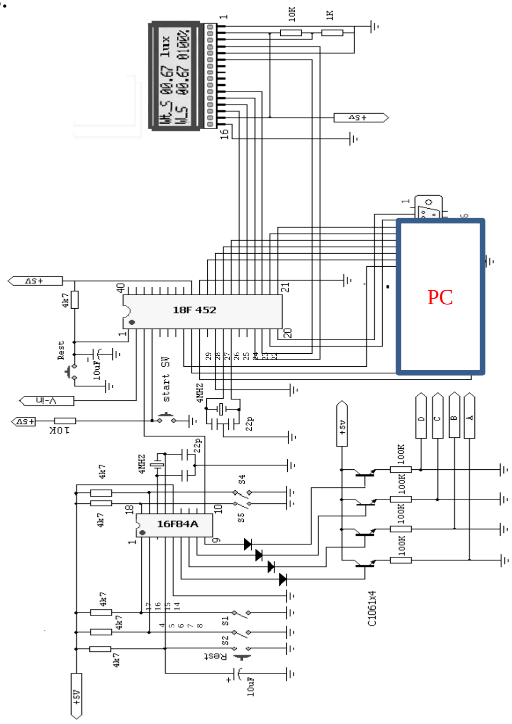

Figure 1. The complete circuit diagram of whole system

3.2 Transducer Unit

The LDR light sensor and the amplifier circuit using Operational Amplifier are designed and constructed. In dark condition (no light falling on the LDR), the value of resistance of the LDR is about 1MΩ and in bright light the value of resistance go down to several hundred ohm.

The value of divider resistor (Rd) has to be chosen to get wider range of light level measurement. For large value of divider resistor Rd = 50kΩ the sensor circuit is very good for sensing in low light level and very poor in the bright light. The sensor circuit work properly in bright light but poor sensitivity for dim light [1] for the low resistance value of Rd=100Ω - 500Ω. The photograph of LDR transducer and motor driver unit and area scanning mechanism are shown in Figure 2(a) and (b).

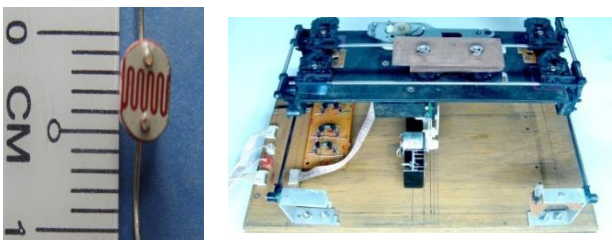

(a) **(b)**

Figure 2. (a) LDR sensor (b) Motor driver unit and mechanism of the area scanning system

3.3 The Light Source Unit

Light source unit consist of eight LED of different color. In construction the light source unit, eight LED are fixed on the plastic disc and each LED is connected the current limiting resistors. The connection of eight LED and their current limiting resistor on the plastic is shown in Figure 3(a). The rotary switch is installed for changing the light source by spinning the plastic disc. The photograph of the constructed light sources unit is described in Figure 3(b).

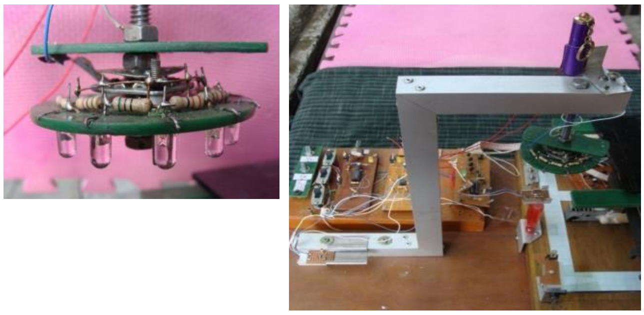

(a) **(b)**

Figure 3. (a) Photograph of light source and (b) Constructed light source unit.

3.3 Microcontroller Based Signal Processing Unit

The measured data produced from transducer circuit (light sensing unit) are analog format. These analog data are converting in to digital form by using analog to digital converter (ADC) which built in PIC18F452 microcontroller [4].

PIC18F452 Microcontroller takes analog ac voltage from the transducer circuit and performs the data acquisition, analog to digital conversion, LCD control and transmission of light intensity calculation, interfacing with personal computer. Crystal (4MHz) and two 22pF capacitor are used for oscillation of microcontroller. Pin2 (RA0/AN0) receives the analog voltage produced by transducer unit and convert it into digital form. A press switch (start switch) was installed between ground and pin4 (RA2) [4] of PIC18F452.

When the high logic level reach at the pin 3 (RA1) [6] from PIC16F48, analog data collecting is start. Firstly without sample data (Wt-S data) is read and store and also display in the LCD display unit. After reading the without sample data, we have to press the start switch (SW5) to send a signal to the motor control unit. The motor control unit starts drive the scanning mechanism and PIC18F452 read the amount of light transmission with sample data (WS-data) for every step moved of glass sample.

The collected data are compared with the without sample data (Wt-S data) and produced the result as percentage of light transmission through the glass sample. It is displayed in second line of LCD display unit. The flow diagram of constructed system is illustrated in Figure 4.

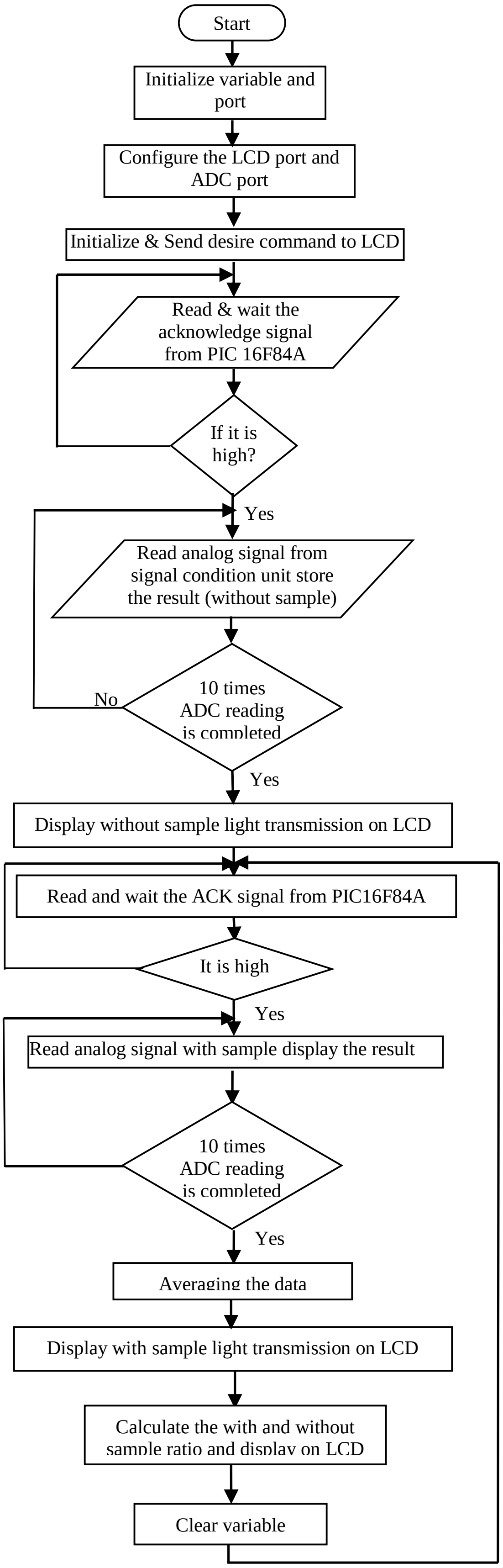

Figure 4. Flow diagram of signal processing program for the MCU18F452

The RC1 to RC7 (PORTC) pins of PIC18F452 are used as digital outputs for driving the LCD display [5]. The RD0 to RD7 (PORTD) of PIC18F452 are used for interfacing with personal computer for displaying the measurement result on the monitor in the form of color mapping diagram. RE0, RE1 and RE2 of PIC18F452 are used for control and handshaking signal in interfacing with computer. All the necessary calculation and digital signal processing and interfacing with computer are done by microcontroller PIC18F452.

A 2×16 type LCD display module is used for displaying the measured result. For reading the result easily from the LCD display back light pin 15 and pin 16 are powering. The first line of LCD display will show the amount of digital quantity (light intensity) without sample condition in LUX unit. Second line displays the digital quantity (light intensity) of transmission of light for with sample in LUX unit and transmission percentage of glass sample from each point of glass sheet.

To view the measure data simply in color pattern on the computer monitor, we have to perform the interfacing with computer. For doing this task we write a program using C# programming langue. The area scanning measurement diagram will be appeared on the monitor in color map. The ten levels of the amount of light transmission % were divided through the glass sample. So, in drawing the color map in the computer ten different colors for each transmission percent were specified. Table 1 shows the used color corresponding to amount of light transmission percent.

Table 1. Specifying the color for different transmission

Sr. No	Amount of light transmission (%)	Used color
0	0 to 10 %	Black
1	11 to 20 %	Brown
2	21 to 30 %	Red
3	31 to 40 %	Orange
4	41 to 50 %	Yellow
5	51 to 60 %	Green
6	61to 70 %	Blue
7	71 to 80 %	Violet
8	81 to 90 %	Gray
9	91 to 100 %	White

4. RESULTS AND DISCUSSION

This research work is intended to develop the microcontroller based light transmission measurement from the specific area of various glass sheets. The amount of transmitted light through the specific area of glass sheet for different color of light sources will be measured and displayed.

The area scanning unit is driven by the PIC16F84A microcontroller. Area 0.5 cm x 0.5 cm is scanned for one data acquisition. When light falling on the light sensor, the transducer unit transforms the light energy into analog voltage. The output voltage of transducer unit is preprocessing by the signal conditioning unit. Firmware embedded in PIC18F452 microcontroller implements the analog to digital conversion for the analog signal, signal processing, displaying the processed results on LCD and interfacing with personal computer (PC).

The two type of display system is applied. A LCD display is used for showing the amount of light intensity without sample (I0), with sample (I) in LUX unit and amount of percent of transmitted light (I/I0) in numerically. PC monitor is used to present transmission percentage of the area scanning result of glass sample in the form of color format.

Three Op_Amps, HA7741IC, are used in an instrumentation amplifier with unity gain. The optimum value of divider resister Rd (1k Ω) is chosen to get wider range of light level. The potential difference produced the LDR is fed to instrumentation amplifier and produce a dc voltage as output. The light intensity falling on LDR is converted into electrical energy (dc voltage) by the transducer circuit. The output voltage of the instrumentation amplifier by changing the input voltage is measured and the characteristic of instrumentation amplifier is shown in Figure 5.

The output analog voltage of the transducer unit by increasing the current (mA) flow through the white LED light source is measured and recorded. Then output voltage (volt) versus current through LED (mA) was plotted and a relation equation was obtained using EXCEL software. The following equation describes the relation between output analog voltage and current.

$$i = 0.265\, e^{2.259v}, \quad (1)$$

i = current through the white LED (mA),

v = output voltage of transducer (V)

Secondly, LDR light sensor is replaced by the sensor of LUX meter without changing the position and distance from light source. In this time the amount of light intensity given by LUX meter was recorded by increasing the current through the white LED light source. After that current (mA) versus light intensity (LUX) will be drawn using the EXCEL application program and the equation that shows the relation between the current and light intensity can be obtained.

The calibration curves and relation equations were generated for various light sources. The output characteristic curve, light intensity versus LED current and calibration curve for each light source were observed and shown in Figure 6(a), (b) and (c) respectively.

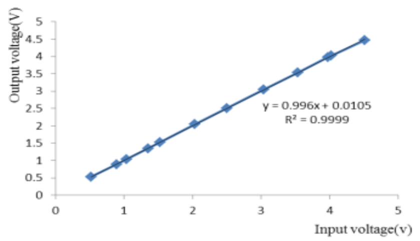

Figure 5. Characteristic curve of instrumentation amplifier

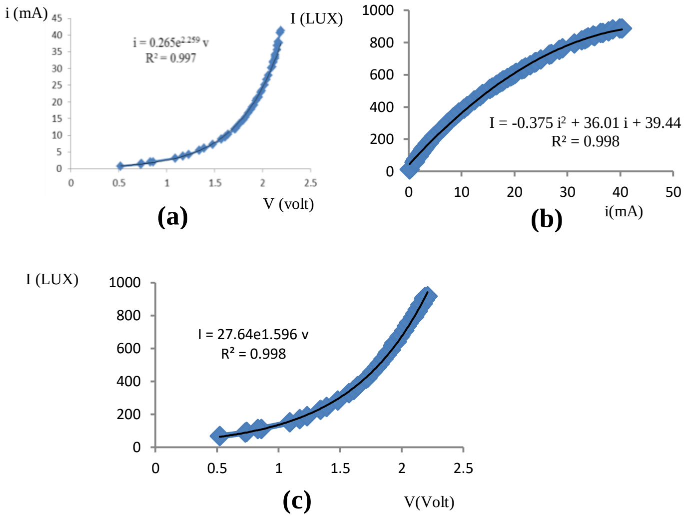

Figure 6. (a) LED current versus output voltage for White LED light source (b) Light intensity versus LED current (c) Calibrated curve drawn by output voltage and light intensity for White LED light source

Investigation of light transmissions on glass samples has been performed by using 8 different colors of LEDs used as light sources. Two main control devices communicate with acknowledge or handshaking signal for precise timing. PIC16F84A sends acknowledge signal after doing its job of scanning unit. PIC18F452 waits this signal and if it gets data acquisition is started.

Output characteristic curves of LDR for white, violet, yellow, green, dark green, blue, red, dark red LEDs were observed and are shown in Figure 7(a), (b), and (c), Figure 8(a), (b), and (c) ,Figure 9(a), (b), and (c), Figure 10(a), (b), and (c) and Figure 11(a), (b), and (c). It is found that the system achieves the wider operating region by using LDR. The calibration equations are tabulated in Table 2.

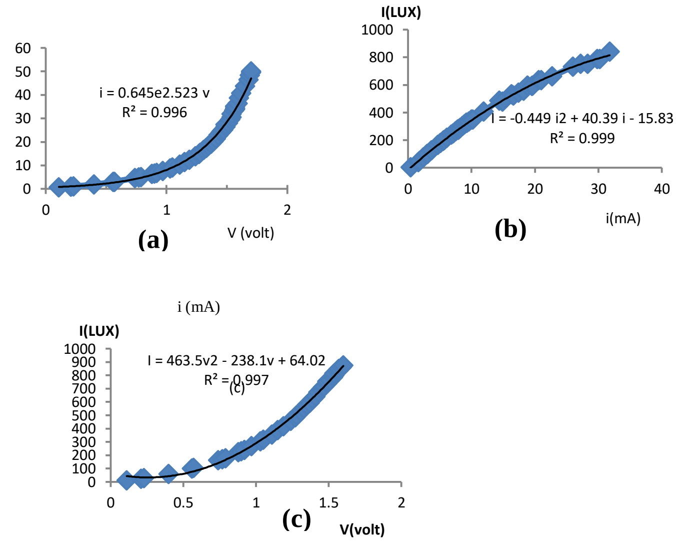

Figure 7. (a) LED current versus output voltage (b) Light intensity versus LED current (c) Calibrated curve drawn by output voltage and light intensity for Violet LED light source

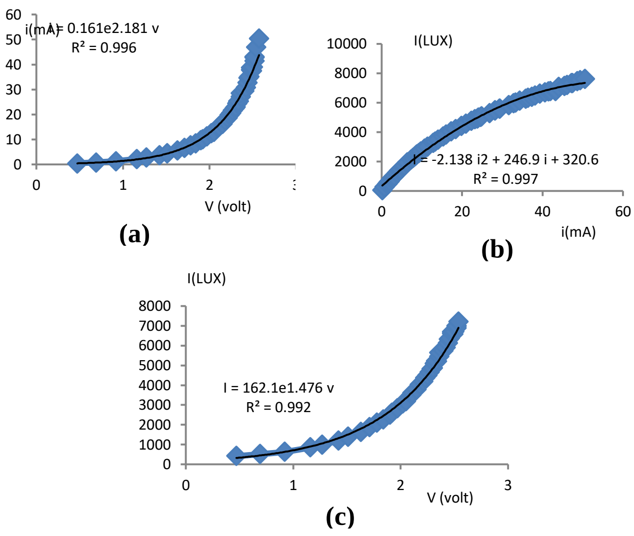

Figure 8. (a) LED current versus output voltage (b) Light intensity versus LED current (c) Calibrated curve drawn by output voltage and light intensity for Blue LED light source

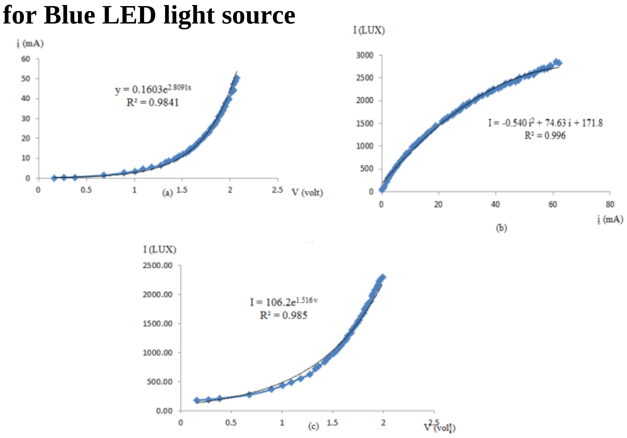

Figure 9. (a) LED current versus output voltage (b) Light intensity versus LED current (c) Calibrated curve drawn by output voltage and light intensity for Green LED light source

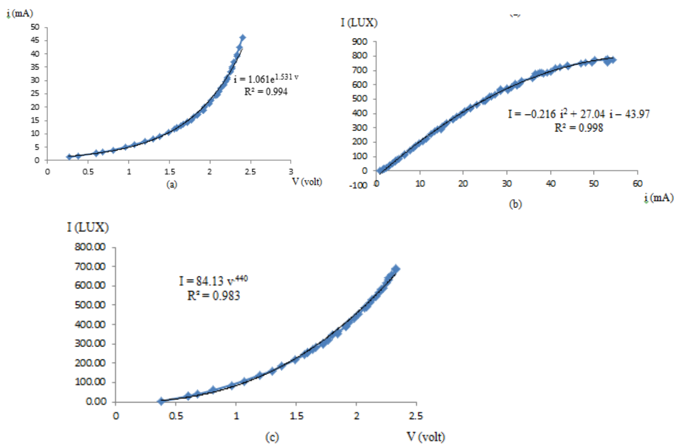

Figure 10. (a) LED current versus output voltage (b) Light intensity versus LED current (c) Calibrated curve drawn by output voltage and light intensity for Yellow LED light source

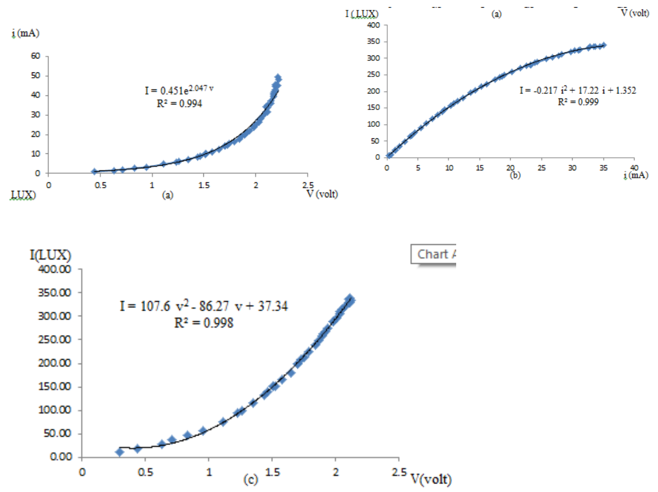

Figure 11. (a) LED current versus output voltage (b) Light intensity versus LED current (c) Calibrated curve drawn by output voltage and light intensity for Red LED light source

The display is shown in Figure 12. Figure 13 shows the photograph of light transmission measurement system. The user interface of the visual C# programming is shown in Figure 14(a). It has three user interface buttons named % and color display, area graph and scanning %. One scanning area in actual size and their respective color can be seen by pressing the % and color display button. Real time area scanning as illustrated in Figure 14(b) can be performed by area graph. Light transmission percentage can be seen by the press of scanning %.

Table 2. Calibrated equations for LDR

Sr. No.	Light Source	Calibrated Equation
1	White LED	$I = 27.64\ e^{1.596\ v}$
2	Violet LED	$I = 463.5v^2 - 238.1v + 64.02$
3	Blue LED	$I = 162.1\ e^{1.476\ v}$
4	Green-1 LED	$I = 106.2\ e^{1.516\ v}$
5	Green-2 LED	$I = 50.44\ e^{1.704\ v}$
6	Yellow LED	$I = 84.13\ v^{.440}$
7	Red-1LED	$I = 107.6\ v^2 - 86.27\ v + 37.34$
8	Red-2 LED	$I = 120.3\ v^2 - 101.7\ v + 44.93$

Figure 12. The output results on the LCD screen

Figure 13. The photograph of the light transmission measurement system

(a) (b)

Figure 14. (a) The user interface of the light transmission software (b) The output screen of the area scanning graph

Some glass samples and their respective area scanning graphs are illustrated in Figure 15(a) and (b), Figure 16(a) and (b).

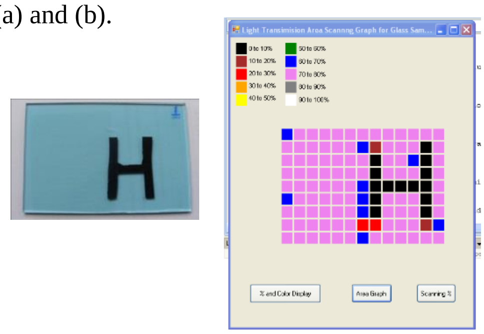

(a) (b)

Figure 15. (a) Glass sample and with H letter (b) Its area scanning graph

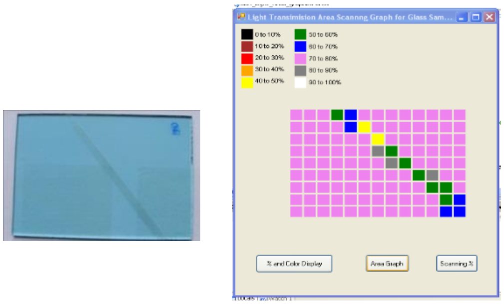

(a) (b)

Figure 16. (a) Glass sample with diagonally defect (b) Its area scanning graph

5. CONCLUSIONS

The microcontroller based light transmission measurement for the specific area of various glass sheets has been designed, programmed and developed. The system can measure transmittance and absorbance of the substance.

In the area scanning unit fine movements of X and Y direction are obtained by using the mechanism of DVD and VCD players. Communications between PIC microcontrollers and Intel Pentium processor are introduced and developed. Programming languages used in each section are different and execution time of their instructions depends on the respective language. Precise timing between different languages and different processors was implemented. Since the system can be used as standalone device it can operate and display the results on LCD display. The PC monitor will only present the graphical display of area scanning. Furthermore the system provides to express transmission percentage in numerically on PC monitor.

Area scanning can be modified with the better special type of mechanism and system sensitivity and reliability can be enhanced. Higher quantity Light source and sensors can produce better performance. The narrow operating region and twice of scanning resolution can be obtained by the use of phototransistor sensor.

ACKNOWLEDGMENT

I would like to express my heartfelt thanks to Dr. Thuya Oo, Rector, Monywa University, for his permission to conduct this work.

REFERENCES

[1] HAMAMATSU Corporation “Application Circuit Example of Si Photodiode”, 360 Foothill Road USA (2004).

[2] T.L. Floyd, "Industrial Electronics", Prentice-Hill Simon & Schuster (Asia) Pte. Ltd., (1997).

[3] F. Stevens, "Getting start with PIC microcontrollers", United State of America (1997).

[4] Microchip Technology Inc., “PIC18F452 Datasheet, 8-Bit CMOS FLASH Microcontrollers,” United State of America (2001) www.microchip.com.

[5] J. Ilett, “How to Use Intelligent L.C.D.s,” Wimbrone Publishing Ltd, New York (1997).

[6] Ad.www.alldatasheet.com/pic16f84A

Certificate Index	***Author***
VOL02IS01001	*Aung Kyi, Zaw Moe Aung* "A Study of Reading Comprehension Questions From Matriculation English Question Papers By Using Bloom’s Taxonomy"
VOL02IS01002	*Aye Aye Lwin, Win Kyaw, Thaik Thaik, San San Wai* "Characterization of Advanced Superionic Conducting Materials of Lithium Cobalt-Nickel Oxides for Solid Oxide Fuel Cell (SOFC) Application"
VOL02IS01003	*Aye Lae Maw* "The Concept of Speech Function in the Articles in the Reader`s Digest"
VOL02IS01004	*Aye Mon Win, Yu Yu Khaing, Lei Yi Htwe* "Performance Analysis of Classification Algorithms in Data Mining Technique"
VOL02IS01005	*Aye Myat Nyo, Day Si Win, Khin Nyein Myint* "Introduction to Popular Hadoop Analytics Tools for Big Data"
VOL02IS01006	*Ei Marlar Win, Shwe Thinzar Aung* "Documents Retrieval using Solr"
VOL02IS01007	*Hla Thein Maung, Aung San Min, Aye Aye Khine* "Construction of Motor Control System Using Fingerprint Sensor"
VOL02IS01008	*Khaing Khin Aye, Thi Thi Swe, Nyein Ei Lwin* မိုးမိုး(အင်းလျား)၏ “မေတ္တာကမ်းနားအချစ်သစ်ပင်”ဝတ္ထုမှ ဇာတ်ဆောင်စရိုက်ဖန်တီးမှု အတတ်ပညာ
VOL02IS01009	*Khaing Su Wai, Hsu Mon Maung* "Analysis of Routing Protocols over TCP in Mobile Ad-hoc Networks using Random Way Point Model"
VOL02IS01010	*Khin Khin Maw* "ဦးပုည၏ တေးထပ်များမှ နှစ်သက်မှုသက်သက်ကိုသာပေးသော ရသမြောက်အဖွဲ့များ လေ့လာချက်"
VOL02IS01011	*Khin Moh Moh Thin, Hla Yin Moe, Lin Lin Aye* "Applying the Queue Theory in Bank Service Centers"
VOL02IS01012	*Khin Pyone, Phyu Phyu Khaing* "ရှင်ဥတ္တမကျော်တောလားလာ ရာသီဘွဲ့၏ သဘောသဘာဝများ လေ့လာချက်"
VOL02IS01013	*Khine Khine* "မြန်မာသဒ္ဒါသမိုင်းကြောင်းလေ့လာချက်"
VOL02IS01014	*May Oo Mon, Su Myat Aye, Naing Naing Maw* "An Investigation into Adolescents’ Emotional Creativity and the Influence of Personality Traits on it"
VOL02IS01015	*May Wah Linn, Naing Naing Maw* "An Investigation into Personality and Career Interest of High School Students"
VOL02IS01016	*Moe Ei Swe, Mar Mar Lwin, Than Than Sint*

University of Computer Studies (Taungoo)
Website: https://ucstaungoo.edu.mm
Email:jites.admin@ucstaungoo.edu.mm

ISBN 978-99971-0-928-6
9 789997 109286 >